2005-03-21

# Equalization Techniques For Multipath Mitigation in Aeronautical Telemetry

Vladimir Ignacio Paje
*Brigham Young University - Provo*

# EQUALIZATION TECHNIQUES FOR MULTIPATH MITIGATION IN AERONAUTICAL TELEMETRY

by

Vladimir Ignacio Paje

A thesis submitted to the faculty of

Brigham Young University

in partial fulfillment of the requirements for the degree of

Master of Science

Department of Electrical and Computer Engineering

Brigham Young University

April 2005

BRIGHAM YOUNG UNIVERSITY

GRADUATE COMMITTEE APPROVAL

of a thesis submitted by

Vladimir Ignacio Paje

This thesis has been read by each member of the following graduate committee and by majority vote has been found to be satisfactory.

| | |
|---|---|
| Date | Michael D. Rice, Chair |
| Date | A. Lee Swindlehurst |
| Date | Wynn C. Stirling |

BRIGHAM YOUNG UNIVERSITY

As chair of the candidate's graduate committee, I have read the thesis of Vladimir Ignacio Paje in its final form and have found that (1) its format, citations, and bibliographical style are consistent and acceptable and fulfill university and department style requirements; (2) its illustrative materials including figures, tables, and charts are in place; and (3) the final manuscript is satisfactory to the graduate committee and is ready for submission to the university library.

Date

Michael D. Rice
Chair, Graduate Committee

Accepted for the Department

Michael A. Jensen
Graduate Coordinator

Accepted for the College

Douglas M. Chabries
Dean, Ira A. Fulton College of Engineering and Technology

# ABSTRACT

## EQUALIZATION TECHNIQUES FOR MULTIPATH MITIGATION IN AERONAUTICAL TELEMETRY

Vladimir Ignacio Paje

Department of Electrical and Computer Engineering

Master of Science

This thesis describes the application of adaptive equalization based on the constant modulus algorithm (CMA) and the decision-feedback minimum mean squared error (DF-MMSE) concept to the two compatible offset QPSK waveforms (FQPSK and SOQPSK-TG) that constitute the ARTM Tier-1 waveforms. An adaptive version of the DF-MMSE equalizer is developed and applied to this application. In the presence of frequency selective multipath interference typically encountered in aeronautical telemetry, both equalization techniques are shown to provide reliable performance for FQPSK and SOQPSK-TG. The performance of both waveforms with the DF-MMSE equalizer is slightly better than that using the CMA equalizer. Implementation trade-offs between the two types of equalizers are discussed.

# ACKNOWLEDGMENTS

I would like to thank my advisor, Dr. Rice, for being a great mentor, and also for his time and patience in helping me write this thesis. I would also like to thank my family and all my friends who have supported me during this endeavor.

# Contents

# List of Tables

## List of Figures

# Chapter 1

# Introduction

The complexity of airborne military systems has increased dramatically over the past 40 years. As a result, the data rates required to test these systems have increased from 100 kbits/sec in the 1970s to 10-20 Mbits/sec today. The consequences of this trend are 1) spectral efficiency has become more important and 2) the multipath interference encountered in aeronautical telemetry has become frequency selective.

The spectral efficiency of PCM/FM, which has been the dominant carrier modulation in aeronautical telemetry for more than 40 years, has proven inadequate. The wide bandwidths required for high data-rate tests have applied tremendous pressure on the spectral allocations at L-band (1435 – 1535 MHz), lower S-band (2200 – 2290 MHz), and upper S-band (2310 – 2390 MHz). The situation was further exacerbated in 1997 when the lower portion of upper S-band from 2310 to 2360 MHz was reallocated in two separate auctions: 2320 – 2345 MHz was reallocated for digital audio radio in one round while 2305 – 2320 MHz and 2345 – 2360 MHz were allocated to wireless communications services in the subsequent rounds.

In response, the Advanced Range Telemetry (ARTM) program [1] was launched by the Central Test and Evaluation Investment Program (CTEIP) in 1997 to identify more bandwidth efficient modulation formats suitable for use in aeronautical telemetry. The goal was to select modulation schemes that required less bandwidth than PCM/FM, but had the same detection efficiency. The severe size and weight restrictions typical of these applications require power amplifiers running full saturation or even class C amplifiers. As a consequence, the search has focused on constant envelope waveforms. New modulation formats were selected in two phases. In the first

phase, a version of the Feher-patented QPSK, called FQPSK [2], was adopted in 2000 as part of the IRIG 106 standard [3]. A compatible variant of the MIL-STD 188-181 Shaped Offset QPSK, called SOQPSK-TG [4], was selected as a compatible alternative in 2004. These two modulations formats, known collectively as the "ARTM Tier-1 Waveforms," have the same detection efficiency as PCM/FM but twice the spectral efficiency as PCM/FM [5], even when used with non-linear power amplifiers. In the second phase, a two index 3RC CPM modulation, described in [6], was selected as the "ARTM Tier-2 Waveform." This waveform, simply called "ARTM CPM" in the 2004 version of IRIG 106, has the same detection efficiency as PCM/FM and approximately 3 times the spectral efficiency of PCM/FM [7].

The second consequence of the increased data rates is the frequency selective nature of the multipath interference. The data links used in aeronautical telemetry are subject to multipath interference in the form of strong "ground bounces" (especially at low elevation angles) and reflections off irregular terrain [8]. At low data rates, such as 100 kbits/sec, the multipath interference appears as flat fading across the signal bandwidth. At high data rates, the signal bandwidth is much wider and the multipath interference is characterized by deep spectral nulls. The frequency selective nature of the multipath interference disrupts the data link and is the main cause of data loss in aeronautical telemetry.

Equalization has been applied as a multipath mitigation technique for several decades [9]. Adaptive equalizers are commonly used since they are able to track changes in the characteristics of the multipath interference. This thesis summarizes an investigation into the performance of adaptive equalizers as a multipath mitigation technique for the ARTM Tier-1 waveforms. The ARTM Tier-1 waveforms are described in Chapter 2 and applicable equalization techniques are described in Chapter 3. Adaptive equalizers based on the constant modulus algorithm (CMA) [10] and the decision feedback minimum mean squared error (DF-MMSE) concept are presented. DF-MMSE equalization for offset modulations was developed by Tu [11]. This thesis extends these concepts to an adaptive solution. BER and MSE test procedures and results are outlined in Chapter 4. Chapter 5 is the conclusion.

# Chapter 2

# Background

The FQPSK and SOQPSK-TG modulation formats (ATRM Tier-1 waveforms) are described in this chapter, with a discussion of possible demodulation schemes. Channel models to characterize the multipath fading environments typical of test ranges in the Western USA have been developed using data collected at Edwards AFB during Winter 1998-1999 [8]. Some of the results of this effort are reproduced in this chapter. These channel models are important for assessing the performance of the equalizers on real channels.

## 2.1 FQPSK and SOQPSK-TG: The ARTM Tier-1 Waveforms

### 2.1.1 FQPSK

#### Description

Feher-patented QPSK (FQPSK) is a variant of offset QPSK where the in-phase and quadrature components of the modulated waveform are cross correlated to produce a quasi-constant envelope signal [12, 13]. Figure 2.1 shows a block diagram of a FQPSK transmitter. The input signal, $d(k)$, consists of data whose values are contained in the set $\{-1, +1\}$. The data is sent through a serial-to-parallel block which separates the original data into in-phase and quadrature data in the following manner:

$$d(k) \in \{-1, +1\} \tag{2.1}$$

$$d_I(n) = d(2k) \tag{2.2}$$

$$d_Q(n) = d(2k+1). \tag{2.3}$$

The separated data points, $d_I(n)$ and $d_Q(n)$, are cross correlated to determine the resultant FQPSK waveforms for both the in-phase and quadrature components. The waveforms may be expressed in terms of a set of 16 baseband pulse shapes $S_i(t); i = 0, 1, 2, \ldots, 15$, with each I and Q component output every half-symbol interval. During the symbol interval $nT_s \leq t \leq (n+1)T_s$, the waveform $S_{i(n)}(t - nT_s)$ is used to amplitude modulate the in-phase component of the carrier. Likewise, during the interval $(n + 1/2)T_s \leq t \leq (n + 3/2)T_s$, the waveform $S_{q(n)}(t - (n + 1/2)T_s)$ is used to amplitude modulate the quadrature component of the carrier. The indices $i(n), q(n) \in \{0, 1, \ldots, 15\}$ are determined by the input data streams and will be described later in this section. The complex baseband FQPSK waveform may be represented as

$$f(t) = \sqrt{E_b} \sum_n \left[ S_{i(n)}(t - nT_s) + jS_{q(n)}(t - (n + 1/2)T_s) \right], \tag{2.4}$$

where $E_b$ is the average bit energy and $T_s$ is the symbol period (or reciprocal of the symbol rate).

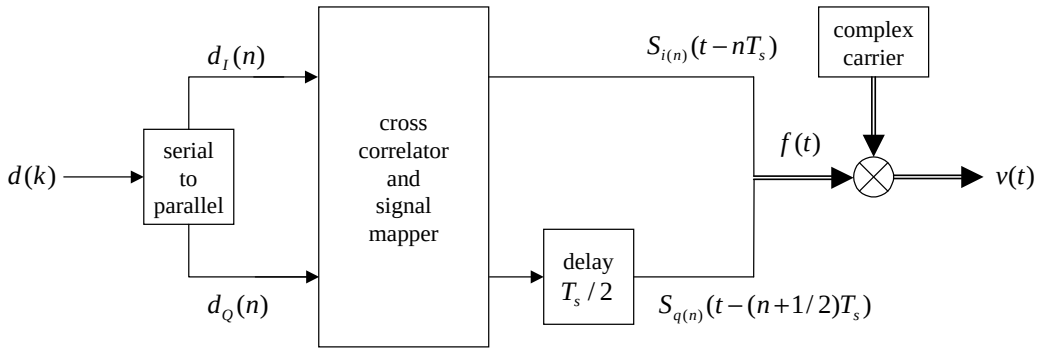


Figure 2.1: FQPSK Transmitter.

The first eight waveforms are defined as follows:

$$S_0(t) = A, \quad 0 \le t \le T_s \tag{2.5}$$

$$S_1(t) = \begin{cases} A, & 0 \le t \le \frac{T_s}{2} \\ 1-(1-A)\cos^2\frac{\pi t}{T_s}, & \frac{T_s}{2} \le t \le T_s \end{cases} \tag{2.6}$$

$$S_2(t) = \begin{cases} 1-(1-A)\cos^2\frac{\pi t}{T_s}, & 0 \le t \le \frac{T_s}{2} \\ A, & \frac{T_s}{2} \le t \le T_s \end{cases} \tag{2.7}$$

$$S_3(t) = 1-(1-A)\cos^2\frac{\pi t}{T_s}, \quad 0 \le t \le T_s \tag{2.8}$$

$$S_4(t) = A\sin\frac{\pi t}{T_s}, \quad 0 \le t \le T_s \tag{2.9}$$

$$S_5(t) = \begin{cases} \sin\frac{\pi t}{T_s}+(1-A)\sin^2\frac{\pi t}{T_s}, & 0 \le t \le \frac{T_s}{2} \\ \sin\frac{\pi t}{T_s}, & \frac{T_s}{2} \le t \le T_s \end{cases} \tag{2.10}$$

$$S_6(t) = \begin{cases} \sin\frac{\pi t}{T_s}, & 0 \le t \le \frac{T_s}{2} \\ \sin\frac{\pi t}{T_s}-(1-A)\sin^2\frac{\pi t}{T_s}, & \frac{T_s}{2} \le t \le T_s \end{cases} \tag{2.11}$$

$$S_7(t) = \sin\frac{\pi t}{T_s}, \quad 0 \le t \le T_s, \tag{2.12}$$

with the other eight waveforms, $S_8(t)$ to $S_{15}(t)$, being the negative of (2.5) to (2.12), respectively.

The particular I and Q waveforms chosen for a specific time interval are based on the most recent data transition on its own channel as well as the two most recent successive transitions on the other channel. From (2.4) we define the I-channel transmitted waveform $S_{i(n)}(t-nT_s)$ in the $n$-th signaling interval $nT_s \le t \le (n+1)T_s$ in terms of the transition properties of the I and Q data symbol sequences $d_I(n)$ and $d_Q(n)$, respectively, with possible values of the data being $\pm 1$.

The mapping conditions can be summarized in a concise form described by Table 2.1. The first column shows the "transition distance" between the current and previous I-channel symbols, $d_I(n)$ and $d_I(n-1)$, respectively. If there is no transition

between the two data symbols, the resultant distance is a 0. If there is a transition (from +1 to -1, or vice versa), the resultant distance is a 1. The next two columns show the "transition distances" of the two most recent successive transitions of the Q-channel symbols, from $d_Q(n-2)$ to $d_Q(n-1)$, and from $d_Q(n-1)$ to $d_Q(n)$, respectively. The last column on the right determines the resultant waveform chosen to be the I-channel baseband signal, $S_{i(n)}(t-nT_s)$. Only the first eight waveforms are listed since the data point $d_I(n)$ of the $n$-th interval determines the sign of the waveform. As an example, if all the specified I and Q transition distances results in 0, meaning no transitions in the defined intervals, then this satisfies the condition shown on the first row in Table 2.1, and the resultant output I-channel waveform $S_{i(n)}(t-nT_s)$ is chosen to be $d_I(n)S_0(t-nT_s)$. This can be shown as the following:

$$S_{i(n)}(t-nT_s) = \begin{cases} S_0(t-nT_s), & \text{for } d_I(n)=1 \\ -S_0(t-nT_s) = S_8(t-nT_s), & \text{for } d_I(n)=-1. \end{cases} \tag{2.13}$$

Table 2.2 shows a similar summary that determines the Q-channel output, $S_{q(n)}(t-(n+1/2)T_s)$, in the $n$-th signaling interval $(n+1/2)T_s \le t \le (n+3/2)T_s$ in terms of the transition properties of the I and Q data symbol sequences $d_I(n)$ and $d_Q(n)$. Figure 2.2 shows the eye diagram of an FQPSK transmission.

**Detection**

The optimal detector is a sequence detector using a trellis that accounts for the possible combinations of waveforms determined by the memory of the waveform mapper [13]. In practice, symbol-by-symbol detection is used since this type of detector is compatible with generic offset QPSK and shaped offset QPSK [3]. This is desireable since the same detector can be used for both waveforms. The symbol-by-symbol detector is illustrated in Figure 2.3. After rotation by the carrier phase synchronizer, the received waveform is filtered by a detection filter with impulse response $g(t)$. Integrate-and-dump detection is realized when $g(t)=1$ for $0 \le t \le T_s$ and 0 otherwise. Simon [13] showed that use of a detection filter matched to the average of the 8 possible waveforms is approximately 1/2 dB better than the integrate-and-dump

Table 2.1: Mapping for I-channel baseband signal $S_{i(n)}(t-nT_s)$ in the interval $nT_s \leq t \leq (n+1)T_s$

| $\frac{d_I(n)-d_I(n-1)}{2}$ | $\frac{d_Q(n-1)-d_Q(n-2)}{2}$ | $\frac{d_Q(n)-d_Q(n-1)}{2}$ | $S_{i(n)}(t-nT_s)$ |
|---|---|---|---|
| 0 | 0 | 0 | $d_I(n)S_0(t-nT_s)$ |
| 0 | 0 | 1 | $d_I(n)S_1(t-nT_s)$ |
| 0 | 1 | 0 | $d_I(n)S_2(t-nT_s)$ |
| 0 | 1 | 1 | $d_I(n)S_3(t-nT_s)$ |
| 1 | 0 | 0 | $d_I(n)S_4(t-nT_s)$ |
| 1 | 0 | 1 | $d_I(n)S_5(t-nT_s)$ |
| 1 | 1 | 0 | $d_I(n)S_6(t-nT_s)$ |
| 1 | 1 | 1 | $d_I(n)S_7(t-nT_s)$ |

Table 2.2: Mapping for Q-channel baseband signal $S_{q(n)}(t-(n+1/2)T_s)$ in the interval $(n+1/2)T_s \leq t \leq (n+3/2)T_s$

| $\frac{d_Q(n)-d_Q(n-1)}{2}$ | $\frac{d_I(n-1)-d_I(n-2)}{2}$ | $\frac{d_I(n)-d_I(n-1)}{2}$ | $S_{q(n)}(t-(n+1/2)T_s)$ |
|---|---|---|---|
| 0 | 0 | 0 | $d_Q(n)S_0(t-(n+1/2)T_s)$ |
| 0 | 0 | 1 | $d_Q(n)S_1(t-(n+1/2)T_s)$ |
| 0 | 1 | 0 | $d_Q(n)S_2(t-(n+1/2)T_s)$ |
| 0 | 1 | 1 | $d_Q(n)S_3(t-(n+1/2)T_s)$ |
| 1 | 0 | 0 | $d_Q(n)S_4(t-(n+1/2)T_s)$ |
| 1 | 0 | 1 | $d_Q(n)S_5(t-(n+1/2)T_s)$ |
| 1 | 1 | 0 | $d_Q(n)S_6(t-(n+1/2)T_s)$ |
| 1 | 1 | 1 | $d_Q(n)S_7(t-(n+1/2)T_s)$ |

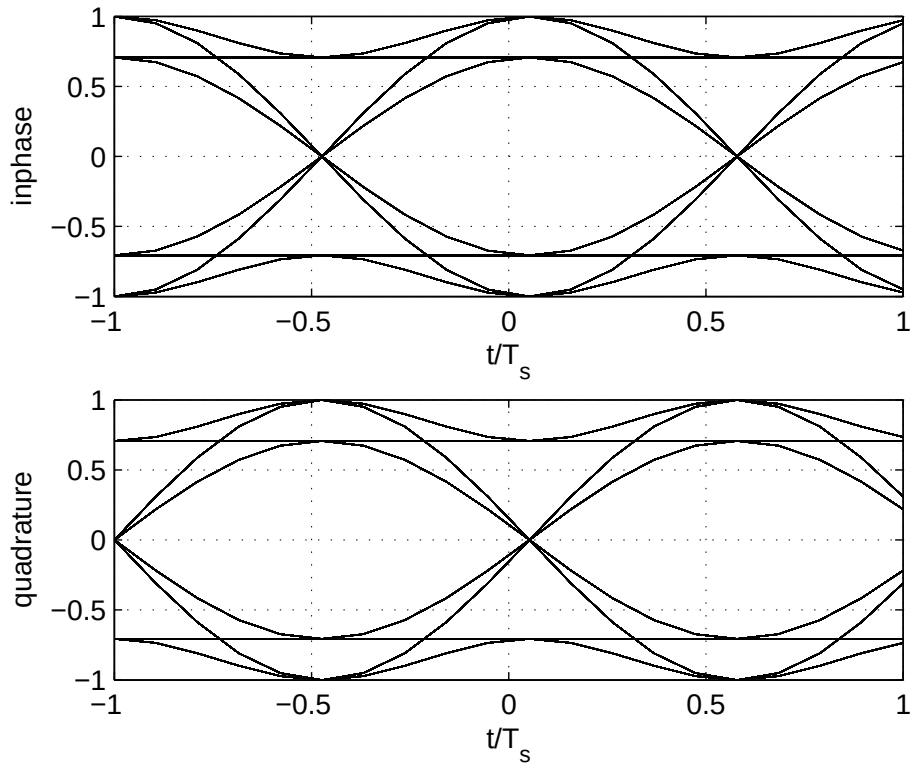


Figure 2.2: Eye diagram for FQPSK.

detection filter in the AWGN environment. (The trellis detector is about 1 dB better than the symbol-by-symbol detector using a detection filter matched to the average of the pulse shapes.) For the simulations in this thesis, an integrate-and-dump detection was used. An I-Q plot of the detector is shown in Figure 2.4.

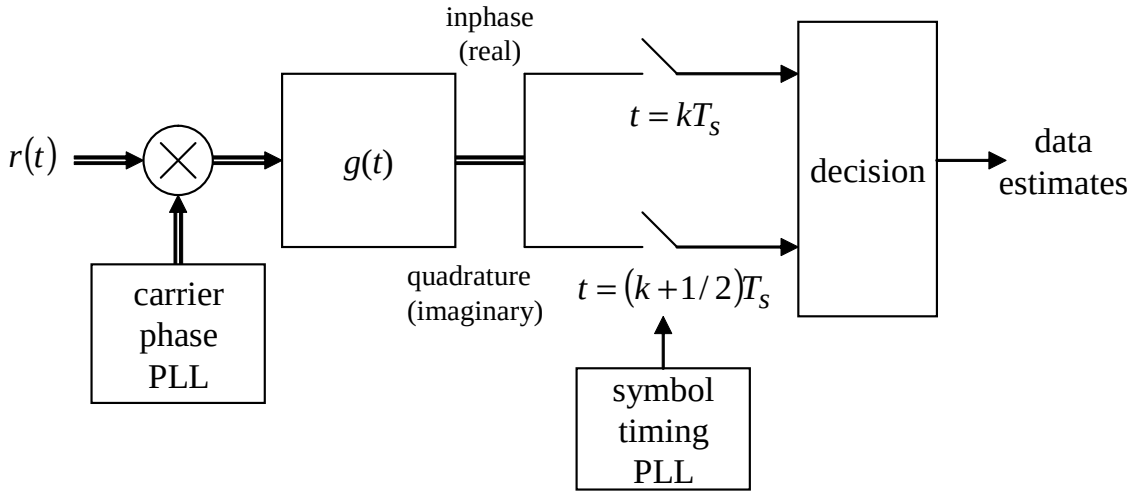


Figure 2.3: Symbol-by-symbol detector for FQPSK and SOQPSK using a simple detection filter.

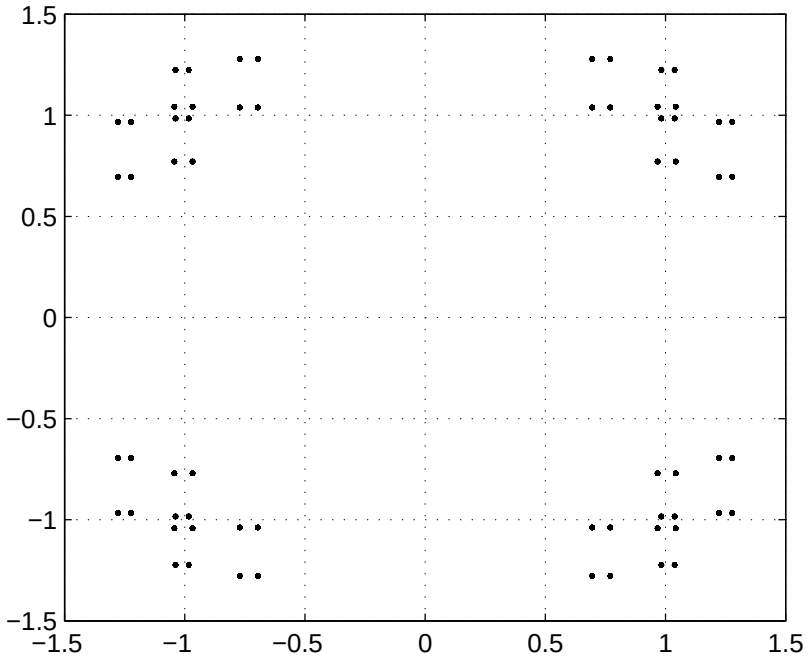


Figure 2.4: I-Q decision points for FQPSK using integrate-and-dump detection.

### 2.1.2 SOQPSK-TG

#### Description

Shaped Offset QPSK (SOQPSK) is a ternary CPM modulation format with modulation index $h = 1/2$. Figure 2.5 shows a block diagram of a SOQPSK transmitter. Using complex baseband notation, the SOQPSK waveform may be represented as

$$s(t) = \exp\{j\phi(t)\} \tag{2.14}$$

$$\phi(t) = \pi \sum_{k} \alpha(k) g(t - kT_b), \tag{2.15}$$

where $\alpha(k) \in \{-1, 0, +1\}$ is the $k$-th ternary symbol, $T_b$ is the bit time, and $g(t)$ is a phase pulse that is the time integral of a frequency pulse $p(t)$ with area 1/2. The frequency pulse defined in MIL-STD 188-181 is a rectangular pulse with duration $T_b$ and amplitude $T_b/2$. IRIG 106-104 specifies a more bandwidth efficient variation of this waveform which it terms SOQPSK-TG. The frequency pulse for SOQPSK-TG is a *spectral* raised-cosine pulse that has been windowed by a *temporal* raised-cosine pulse. The phase and frequency pulses for SOQPSK-TG are given by [4]

$$g(t) = \int_{-\infty}^{t} p(x)dx \tag{2.16}$$

$$p(t) = A \frac{\cos\left(\frac{\pi\rho Bt}{2T_b}\right)}{1 - 4\left(\frac{\rho Bt}{2T_b}\right)^2} \times \frac{\sin\left(\frac{\pi Bt}{2T_b}\right)}{\frac{\pi Bt}{2T_b}} \times w_n(t), \tag{2.17}$$

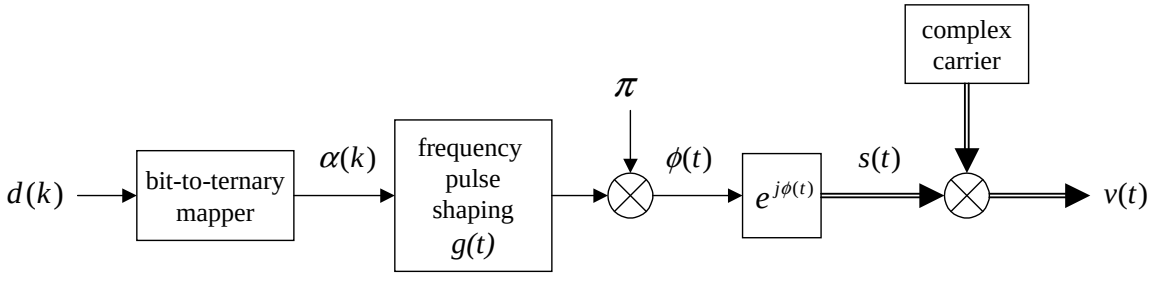


Figure 2.5: SOQPSK Transmitter.

where the window is

$$w_n(t) = \begin{cases} 1 & 0 \leq \left|\frac{t}{2T_b}\right| \leq T_1 \\ \frac{1}{2} + \frac{1}{2}\cos\left(\frac{\pi}{T_b}\left(\frac{t}{2T_b} - T_1\right)\right) & T_1 \leq \left|\frac{t}{2T_b}\right| \leq T_1 + T_2 \\ 0 & T_1 + T_2 \leq \left|\frac{t}{2T_b}\right| \end{cases} \tag{2.18}$$

and the constant A is chosen to make the area of $p(t)$ 1/2. The waveform is completely specified by the parameters $\rho$, $B$, $T_1$, and $T_2$. The original publication [4] presented two versions: SOQPSK-A defined by $\rho = 1$, $B = 1$, $T_1 = 1.35$, and $T_2 = 1.4$ and SOQPSK-B defined by $\rho = 0.7$, $B = 1.5$, $T_1 = 1.5$, and $T_2 = 0.5$. SOQPSK-A has a slightly narrower bandwidth (measured at the -60 dB level) and slightly worse detection efficiency than SOQPSK-B. The Telemetry Group of the Range Commanders Council adopted a compromise waveform designated SOQPSK-TG in 2003. The values for SOQPSK-TG are $\rho = 0.7$, $B = 1.25$, $T_1 = 1.5$, and $T_2 = 0.5$. The frequency pulse has support on the interval $-4 \leq t/T_b \leq 4$ and thus spans 4 signaling intervals. SOQPSK-TG is an example of *partial response* CPM [14]. The mapping from bits to ternary symbols is described as follows [4]:

$$\alpha(k) = (-1)^{k+1}\frac{d(k-1)\left[d(k) - d(k-2)\right]}{2}, \tag{2.19}$$

where $d(k) \in \{+1, -1\}$ is the $k$-th data bits.

The name "shaped offset QPSK" follows from the observation that each ternary symbol causes the carrier phase to either advance by $\pm\pi/2$ radians or remain at its current value. When viewed on an I-Q plot, the carrier phase appears to migrate from quadrant to quadrant along the unit circle, giving the appearance of an offset QPSK whose phase transitions have been "shaped." An eye diagram of the SOQPSK-TG transmission is shown in Figure 2.9.

### Detection

The optimum SOQPSK-TG detector is a trellis detector that tracks the possible phase trajectories as described in [14]. As before, the symbol-by-symbol detector like the one illustrated in Figure 2.3 is used for compatibility. The I-Q plot for

SOQPSK-TG detection is shown in Figure 2.6. Detection filters for SOQPSK-TG have been studied by Geoghegan, et. al. [15], using experimental techniques.

## 2.2 Multipath LTI Model

Aeronautical telemetry channels are time-varying since the aircraft is constantly moving. The channel impulse response is a function of the physical geometry of the airborne transmitter, the ground-based receiver, and the surrounding environment. Multipath fading occurs when copies of the transmitted signal are received with the line-of-sight (LOS) transmission. The extra copies of the transmitted signal are usually reflections from fixed landmarks such as mountains, buildings or the ground. The varying nature of the environment causes the reflections to arrive at random times and phases, which results in constructive or destructive interference. The fading that occurs during destructive interference can either be flat or frequency-selective.

We assume that over a short period of time the environment can be considered static, and thus the multipath interference can be modeled as a linear time-invariant (LTI) system. The impulse response is given by the following general equation:

$$h(t) = \delta(t) + \sum_{k=1}^{L-1} \Gamma_k e^{-j\omega_c \tau_k} \delta(t - \tau_k), \tag{2.20}$$

where $\delta(t)$ is the line-of-sight component and the term following the summation represents the $L-1$ copies of the received signal, where $\Gamma_k$ is the complex gain of the $k$-th propagation path, $\tau_k$ is the propagation delay of the $k$-th propagation path, and $\omega_c$ is the RF carrier frequency. The parameters $\Gamma_k$ and $\tau_k$ are normalized to the line-of-sight component. Thus, $\tau_k$ will always be positive because the LOS transmission travels the shortest distance to the receive antenna and arrives first. Also, since the power of the reflected signal is diminished, $|\Gamma_k|$ is bounded by the values $0 < |\Gamma_k| < 1$.

### 2.2.1 The Three Ray Model

Channel modeling experiments described in [8] show that $L = 3$ is an adequate model. The impulse response for the three ray model is

$$h(t) = \delta(t) + \Gamma_1 e^{-j\omega_c \tau_1} \delta(t - \tau_1) + \Gamma_2 e^{-j\omega_c \tau_2} \delta(t - \tau_2). \tag{2.21}$$

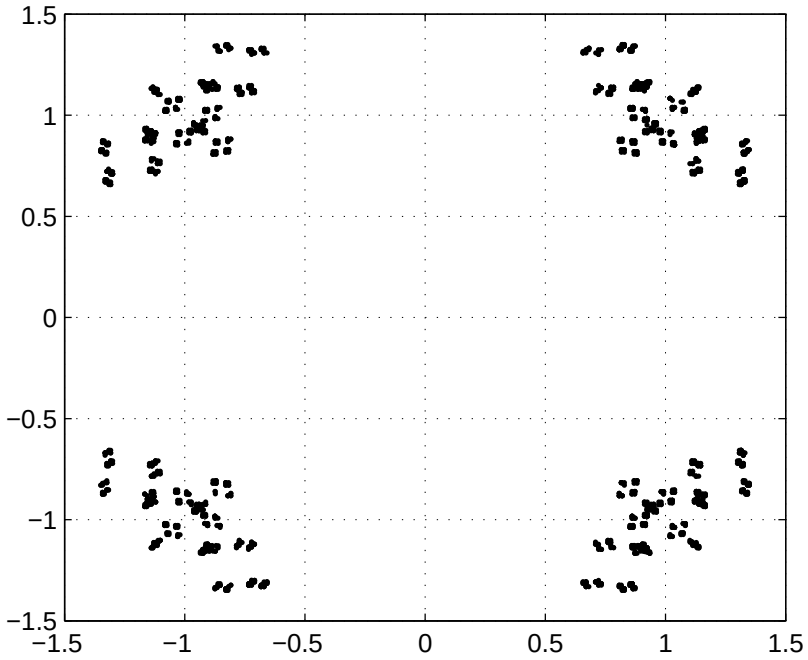


Figure 2.6: I-Q decision points for SOQPSK-TG using integrate-and-dump detection.

The corresponding channel transfer function is

$$H(\omega) = 1 + \Gamma_1 e^{-j(\omega\tau_1+\omega_c\tau_1)} + \Gamma_2 e^{-j(\omega\tau_2+\omega_c\tau_2)}. \tag{2.22}$$

The first specular reflection is characterized by a relative amplitude of 70% to 96% of the line-of-sight amplitude and a delay of 10-80 ns. This path is the result of "ground bounces" off the dry lake bed at Edwards and is a typical terrain feature at DoD test ranges located in the western United States.

### 2.2.2 Multipath Example

The effect of frequency selective multipath interference is illustrated in Figures 2.7 and 2.8 for the case of a channel impulse response given by

$$h(t) = \delta(t) + 0.8e^{j6\pi/5}\delta(t - 45 \times 10^{-9}) + 0.01e^{j\pi}\delta(t - 155 \times 10^{-9}). \tag{2.23}$$

These are typical of the values measured at Edwards AFB, California. Figure 2.8 is a plot of the channel transfer function. Note the spectral null with 3-dB bandwidth

$$W_{3dB} = \frac{1 - \frac{1}{\pi}\cos^{-1}\left(\frac{1-2(1+|\Gamma_1|^2)}{4|\Gamma_1|}\right)}{\tau_1} = 5.5\text{MHz} \tag{2.24}$$

and depth

$$D = -20\log_{10}(1 - |\Gamma_1|) = 14\text{dB}. \tag{2.25}$$

The frequency at which the spectral null occurs is determined by the phase of $\Gamma_1$ and the product of the delay $\tau_1$ and the carrier frequency as described in [8]. The effect of this channel on 20 Mbit/sec SOQPSK-TG is shown in Figure 2.8. Note the spectral null in the received spectrum just above the carrier. The frequency selective multipath has a profound impact on the bit error rate performance of the signal. This is illustrated by the eye diagrams for 20 Mbit/sec SOQPSK-TG shown in Figures 2.9 and 2.10. For reference, the eye diagram for the case of no multipath interference is shown in Figure 2.9. Observe that in Figure 2.10 the multipath distortion essentially closes the eye, rendering reliable detection almost impossible.

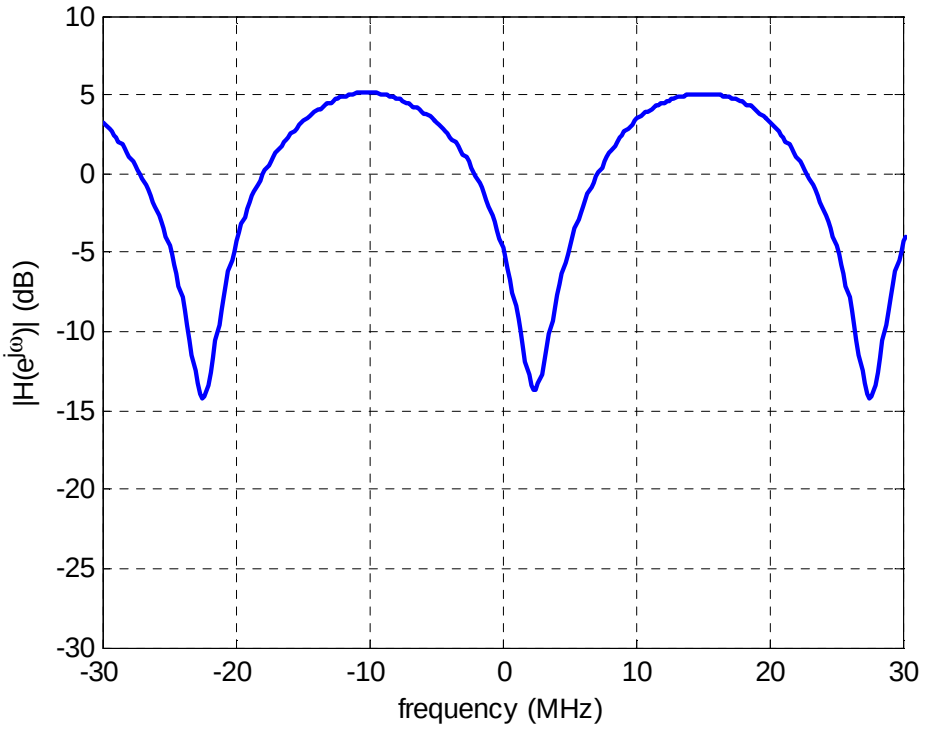


Figure 2.7: Channel transfer function corresponding to the channel impulse response (2.23).

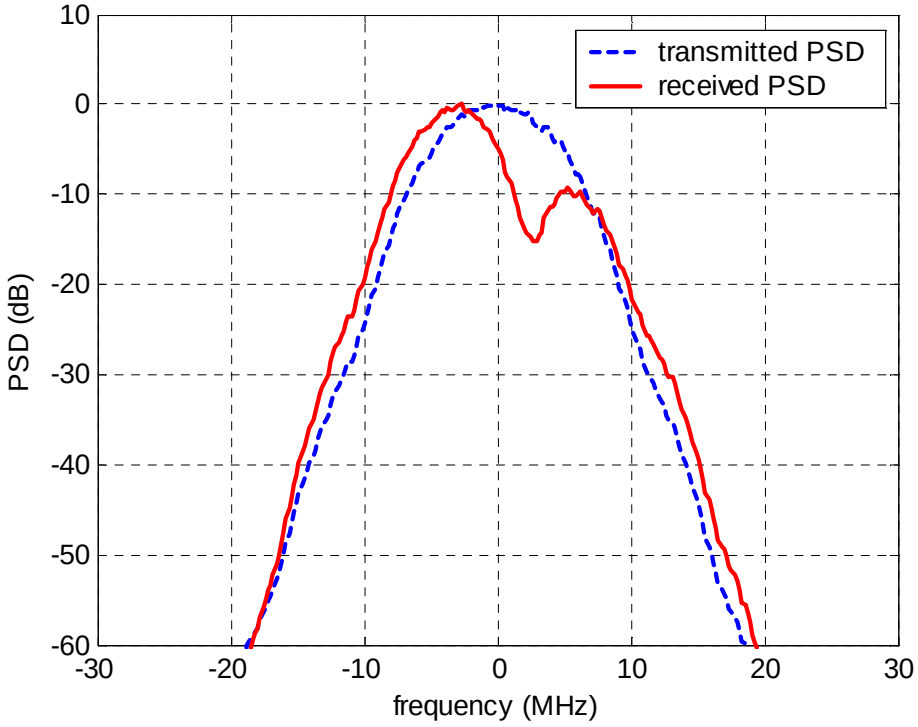


Figure 2.8: The effect of (2.23) channel on the spectrum of 20 Mbit/sec SOQPSK-TG.

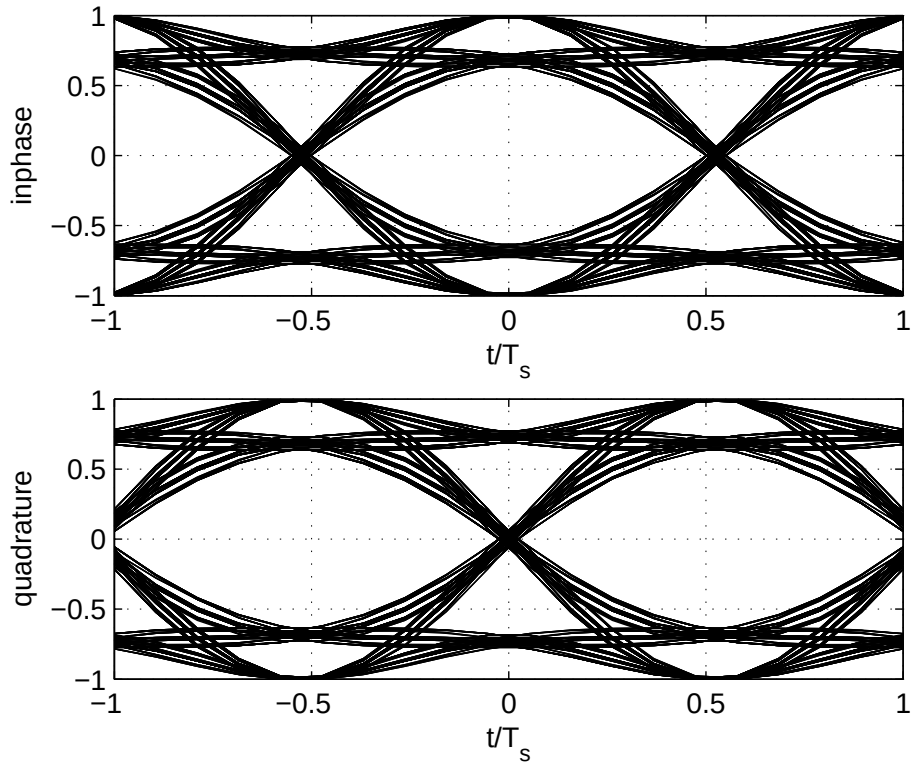


Figure 2.9: Eye diagram for SOQPSK-TG for the case of no multipath.

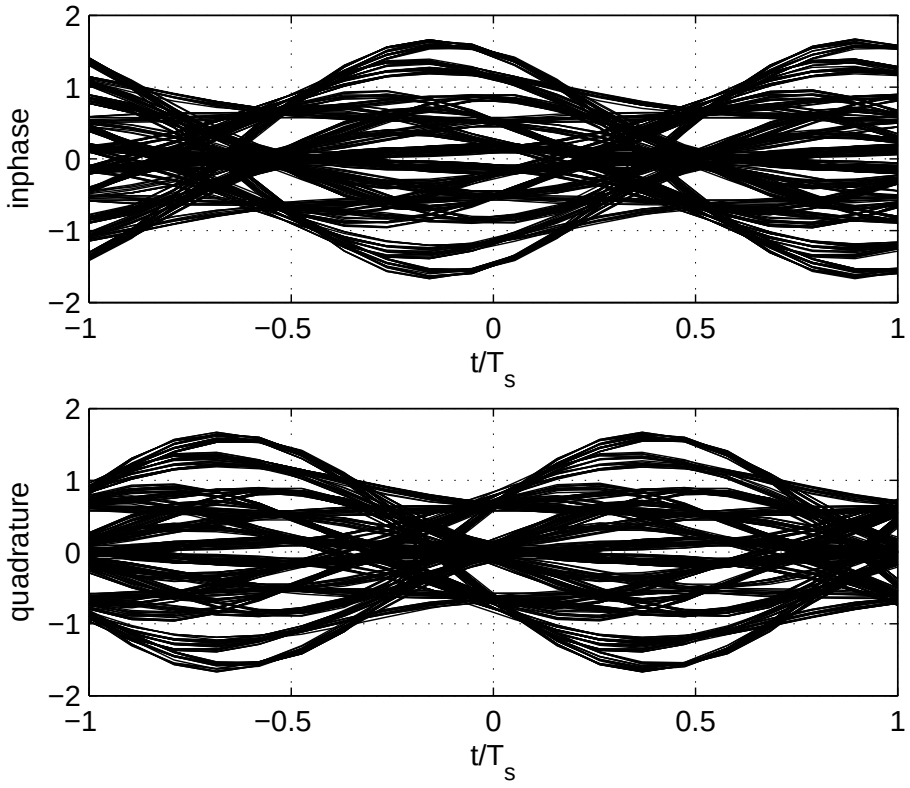


Figure 2.10: Eye diagram for SOQPSK-TG for the case of multipath interference given by the channel impulse response (2.23).

# Chapter 3

# Equalizers

Two equalizers are investigated for the mitigation of multipath fading. The first equalizer is the Constant Modulus Algorithm, or CMA [10]. The CMA equalizer uses *a priori* knowledge about the transmitted waveform to develop an adaptive finite impulse response filter. In the case of FQPSK and SOQPSK-TG, the transmitted signal has a constant modulus. Hence, the CMA is a natural choice for the ARTM Tier-1 waveforms because they have a constant envelope. The second equalizer is the optimum MMSE equalizer for offset modulation with decision feedback (DF-MMSE). The DF-MMSE equalizer uses the offset nature of the signal to minimize the error on each quadrature separately. This characteristic also makes the DF-MMSE equalizer a good choice for ARTM Tier-1 waveforms, because the in-phase and quadrature data output from the detection filter of an FQPSK or SOQPSK-TG demodulator is naturally offset. This chapter will explain the mathematical development of each equalizer as it is implemented as part of the demodulator.

## 3.1 Constant Modulus Algorithm Equalizer

The equalizers based on CMA are a special case of blind equalization techniques that do not require knowledge of the data symbols or timing synchronization. Since the CMA equalizer is blind, it may be inserted prior to the detector of Figure 2.3. However, it is common for the CMA equalizer to be inserted after the carrier phase-locked loop so that the equalizer can operate at baseband. Figure 3.1 shows the symbol-by-symbol detector with the inserted CMA equalizer. The received complex

baseband waveform $r(t)$ is sampled every $T$ seconds to provide samples at a normalized rate of $N = T_s/T$ samples/symbol. The output of the CMA filter $y(n)$ is given as

$$y(n) = \mathbf{r}^T(n)\mathbf{w}, \tag{3.1}$$

where $\mathbf{r}(n)$ is a vector of the most recent $L$ samples of $r(t)$

$$\mathbf{r}(n) = \begin{bmatrix} r(n) \\ r(n-1) \\ \cdots \\ r(n-L+1) \end{bmatrix} \tag{3.2}$$

and $\mathbf{w}$ is the vector coefficients, given by

$$\mathbf{w} = \begin{bmatrix} w(0) \\ w(1) \\ \cdots \\ w(L-1) \end{bmatrix}, \tag{3.3}$$

with $n$ being the time index, and $L$ being the filter length. The filter coefficients are chosen to minimize

$$J = \frac{1}{4}E\{[|y(n)|^2 - 1]^2\}, \tag{3.4}$$

where $E$ denotes expectation. The objective in choosing $\mathbf{w}$ is to minimize $J$ and in the process make $y(n)$ as close to unit length (constant modulus) as possible. The

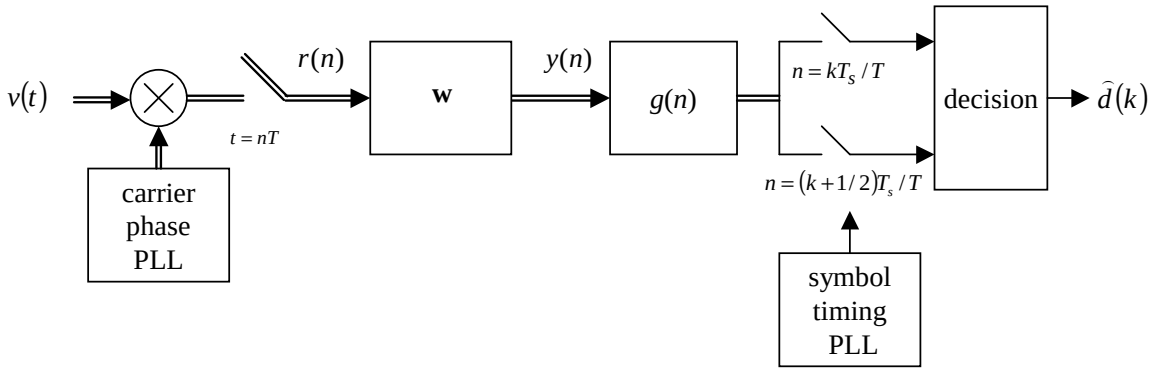


Figure 3.1: Symbol-by-symbol detector with inserted CMA equalizer.

necessary condition for $\mathbf{w}$ is

$$\nabla_{\mathbf{w}} J = 0, \tag{3.5}$$

where $\nabla_{\mathbf{w}}$ is the gradient operator with respect to $\mathbf{w}$. Solving (3.5) reveals the following:

$$\begin{aligned}
\nabla_{\mathbf{w}} J &= \nabla_{\mathbf{w}} \frac{1}{4} E\{[|y(n)|^2 - 1]^2\} \\
0 &= \frac{1}{2} E\{[|y(n)|^2 - 1] \nabla_{\mathbf{w}} |y(n)|^2\} \\
0 &= \frac{1}{2} E\{[\mathbf{w}^H \mathbf{r}^*(n) \mathbf{r}^T(n) \mathbf{w} - 1] \nabla_{\mathbf{w}} [\mathbf{w}^H \mathbf{r}^*(n) \mathbf{r}^T(n) \mathbf{w}]\} \\
0 &= E\{[\mathbf{w}^H \mathbf{r}^*(n) \mathbf{r}^T(n) \mathbf{w} - 1] \mathbf{r}^*(n) \mathbf{r}^T(n) \mathbf{w}\} \\
0 &= E\{[\mathbf{w}^H \mathbf{r}^*(n) \mathbf{r}^T(n) \mathbf{w} \mathbf{r}^*(n) \mathbf{r}^T(n) \mathbf{w} - \mathbf{r}^*(n) \mathbf{r}^T(n) \mathbf{w}]\}.
\end{aligned} \tag{3.6}$$

The closed form solution to minimize $J$ requires knowledge of the 4th moment of $\mathbf{r}(n)$. In general, this is not known, so we use an iterative approach based on gradient descent. The coefficients are updated by a simple gradient search algorithm to minimize $J$ according to the following equation:

$$\mathbf{w}^{(n+1)} = \mathbf{w}^{(n)} - \mu \nabla_{\mathbf{w}} J, \tag{3.7}$$

where $\mu$ is the step size. For use in the gradient search algorithm, $\nabla_{\mathbf{w}} J$ may be expressed in the more useful form:

$$\begin{aligned}
\nabla_{\mathbf{w}} J &= \nabla_{\mathbf{w}} \frac{1}{4} E\{[|y(n)|^2 - 1]^2\} \\
&= \frac{1}{2} E\{[|y(n)|^2 - 1] \nabla_{\mathbf{w}} |y(n)|^2\} \\
&= \frac{1}{2} E\{[|y(n)|^2 - 1] \nabla_{\mathbf{w}} [\mathbf{w}^H \mathbf{r}^*(n) \mathbf{r}^T(n) \mathbf{w}]\} \\
&= E\{[|y(n)|^2 - 1] \mathbf{r}^*(n) \mathbf{r}^T(n) \mathbf{w}\} \\
&= E\{[|y(n)|^2 - 1] y(n) \mathbf{r}^*(n)\}.
\end{aligned} \tag{3.8}$$

The adaptive algorithm is obtained by replacing the true gradient of (3.8) with an instantaneous gradient estimate, or one point average, given as

$$\hat{\nabla}_{\mathbf{w}} J = [|y(n)|^2 - 1] y(n) \mathbf{r}^*(n). \tag{3.9}$$

Substituting the instantaneous gradient estimate into 3.7 yields the desired algorithm

$$\mathbf{w}^{(n+1)} = \mathbf{w}^{(n)} - \mu e(n)\mathbf{r}^*(n), \tag{3.10}$$

where the error term $e(n)$ is defined to be

$$e(n) = [|y(n)|^2 - 1]y(n) \tag{3.11}$$

and $\mu$ is an adjustable step size parameter that controls convergence and steady state error variance [16]. Figure 3.2 shows the new block diagram of the symbol detector and CMA equalizer with filter tap updates realized by (3.10).

Several benefits arise for using the CMA filter for equalization. Since a training signal is not needed, the demodulator does not need to have an established communications link with the transmitter, thus allowing the transmitter to operate normally without losing time to train the receiver [17]. Also, since the CMA algorithm is phase-invariant [10], the blind equalization can operate without the need for carrier acquisition. The carrier tracking loop can then be implemented with low loop delay, speeding up acquisition and improving its tracking rate, a benefit for time varying signals. The CMA equalizer must operate at a sample rate large enough to satisfy the Nyquist sampling theorem.

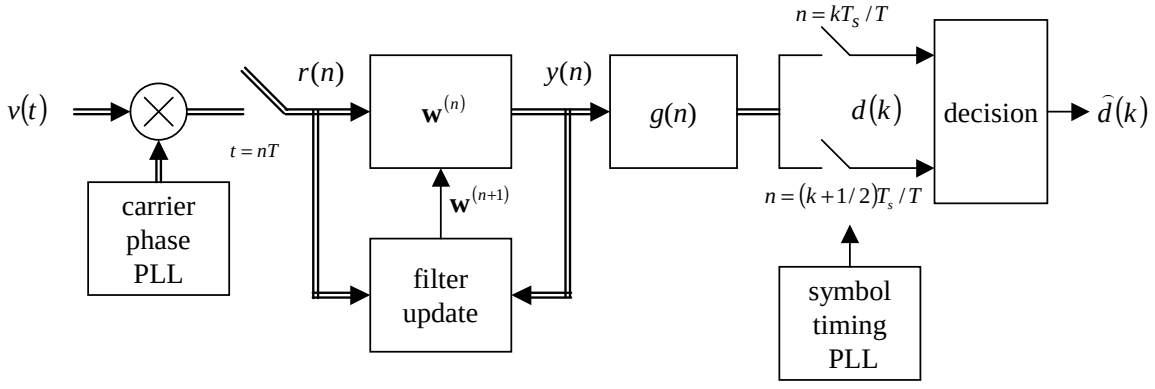


Figure 3.2: Symbol-by-symbol detector with CMA equalizer showing the filter tap update according to (3.10).

## 3.2 Decision Feedback Minimum Mean Squared Error Equalizer

The DF-MMSE Equalizer takes advantage of the offset nature of the FQPSK and SOQPSK-TG modulation. Traditional equalization, designed for non-offset modulations, are suboptimal for offset modulation because it places unnecessary restrictions on the equalizer output. So, instead of placing constraints on both dimensions of the complex signal at the same time, the DF-MMSE Equalizer computes the minimum mean square solution only for the dimension of interest, and alternate the equalization of signal components from symbol to symbol. The residual error in the unmodulated axis does not contribute to error probability. This equalization based on the decision feedback minimum mean squared error criterion for offset QPSK was developed by Tu [11].

### 3.2.1 Notation

Before deriving the minimum squared error criteria for the DF-MMSE equalizer, we must first define all of the notations. Figure 3.3 shows a block diagram of the DF-MMSE equalizer. The detection filter output $z_d(t)$ is sampled at two samples/symbol. The $n$-th sample is filtered by the FIR feedforward filter with $L_{\mathrm{FF}}$

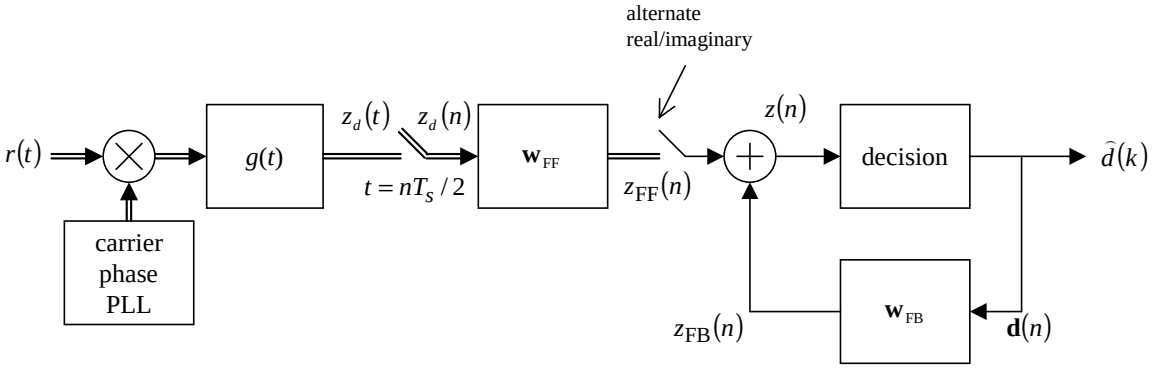


Figure 3.3: Symbol-by-symbol detector with DF-MSEE equalizer.

coefficients $\mathbf{w}_{\mathrm{FF}}$ where

$$\mathbf{w}_{\mathrm{FF}} = \begin{bmatrix} w_{\mathrm{FF}}(-\frac{L_{\mathrm{FF}}-1}{2}) \\ \vdots \\ w_{\mathrm{FF}}(0) \\ \vdots \\ w_{\mathrm{FF}}(\frac{L_{\mathrm{FF}}-1}{2}) \end{bmatrix} \tag{3.12}$$

at time index $n$. The output of the feedforward filter, $z_{\mathrm{FF}}(n)$ is given by

$$z_{\mathrm{FF}}(n) = \mathbf{w}_{\mathrm{FF}}^T \mathbf{z}_d(n), \tag{3.13}$$

where $\mathbf{z}_d(n)$ is a vector of the sampled detection filter output

$$\mathbf{z}_d(n) = \begin{bmatrix} z_d(n + \frac{L_{\mathrm{FF}}-1}{2}) \\ \vdots \\ z_d(n) \\ \vdots \\ z_d(n - \frac{L_{\mathrm{FF}}-1}{2}) \end{bmatrix}. \tag{3.14}$$

This output is combined with the output of the length-$L_{\mathrm{FB}}$ feed back filter, $z_{\mathrm{FB}}$, to form the signal

$$z(n) = z_{\mathrm{FF}}(n) + z_{\mathrm{FB}}(n). \tag{3.15}$$

The output of the feedback filter is given by

$$z_{\mathrm{FB}}(n) = \mathbf{w}_{\mathrm{FB}}^T \mathbf{d}(n), \tag{3.16}$$

where

$$\mathbf{w}_{\mathrm{FB}} = \begin{bmatrix} w_{\mathrm{FB}}(0) \\ w_{\mathrm{FB}}(1) \\ \vdots \\ w_{\mathrm{FB}}(L_{\mathrm{FB}} - 1) \end{bmatrix} \tag{3.17}$$

and $\mathbf{d}(n)$ is based on the decisions. Due to the offset nature of the modulation, symbol decisions are based on samples that alternate between the real and imaginary parts of the feed forward filter output. Assuming the even-indexed samples correspond to

the data sample on the real component and the odd-indexed samples correspond to the data on the imaginary component, $\mathbf{d}(n)$ may be expressed as

$$\mathbf{d}(n) = \begin{cases} \Re\{\hat{d}(k)\}, j\Im\{\hat{d}(k-1)\}, \Re\{\hat{d}(k-2)\}, \ldots \\ \qquad \text{for } n \text{ even and } k = \frac{n}{2} \\ j\Im\{\hat{d}(k)\}, \Re\{\hat{d}(k-1)\}, j\Im\{\hat{d}(k-2)\}, \ldots \\ \qquad \text{for } n \text{ odd and } k = \frac{n-1}{2}, \end{cases} \tag{3.18}$$

where the decisions are

$$\hat{d}(k) = \begin{cases} \text{sgn}\left(\Re\left\{z\left(\frac{n}{2}\right)\right\}\right) & n \text{ even} \\ j\text{sgn}\left(\Im\left\{z\left(\frac{n-1}{2}\right)\right\}\right) & n \text{ odd.} \end{cases} \tag{3.19}$$

The alternating nature of the error signal is the key difference between the MMSE equalization algorithm for offset modulations and non-offset modulations.

### 3.2.2 MSE Criteria

At time $n$, where $n$ is even, we need to consider only the real component of the equalizer error, as the imaginary component is orthogonal to the decision boundary and does not contribute to the error. The filter coefficients are chosen to minimize

$$J = \frac{1}{2}E\left\{\left[\Re\left\{\hat{d}(k) - z(n)\right\}\right]^2\right\}. \tag{3.20}$$

The objective in choosing $\mathbf{w}$ is to minimize $J$ and in the process make $\Re\{z(n)\}$ as close to the magnitude of the decision value $\hat{d}(k)$, which is unit length.

#### Closed Form Solution

Let $s(t)$ be the complex baseband offset transmission represented by

$$s(t) = \sum_k \left[a(k)S_I(t - kT_s) + jb(k)S_Q(t - (k + 1/2)T_s)\right], \tag{3.21}$$

where $a(k)$ and $b(k)$ represent the real and imaginary components of the symbol information at time $k$. We create a vector $\mathbf{x}(n)$ that represents just the symbol information as it is transmitted using a new time index $n$ where $n = 2k$. A vector of

the transmitted signal can be shown as follows:

$$\mathbf{x}(n) = \begin{bmatrix} x\left(n + \frac{L_{\mathrm{FF}}-1}{2}\right) \\ x\left(n + \frac{L_{\mathrm{FF}}-1}{2} - 1\right) \\ x\left(n + \frac{L_{\mathrm{FF}}-1}{2} - 2\right) \\ \cdots \\ x\left(n - L_{\mathrm{h}} - \frac{L_{\mathrm{FF}}-1}{2}\right) \end{bmatrix} = \begin{bmatrix} a\left(\frac{n+\frac{L_{\mathrm{FF}}-1}{2}}{2}\right) \\ jb\left(\frac{n+\frac{L_{\mathrm{FF}}-1}{2}-1}{2} - 1\right) \\ a\left(\frac{n+\frac{L_{\mathrm{FF}}-1}{2}-2}{2}\right) \\ \cdots \\ jb\left(\frac{n-L_{\mathrm{h}}-\frac{L_{\mathrm{FF}}-1}{2}}{2} - 1\right) \end{bmatrix}. \tag{3.22}$$

The transmitted signal passes through a complex-valued channel of length $L_{\mathrm{h}}$, represented by a linear filter $[h_0 \ h_1 \ \cdots \ h_{L_{\mathrm{h}}-1}]$. This channel is a convolution of the transmission waveform generator filter, the multipath environment, and the detection filter at the demodulator. The received signal at the sampled detection filter output $\mathbf{z}_d(n)$ is a convolution of the transmitted signal with the channel and can be represented as the following:

$$\mathbf{z}_d(n) = \mathbf{H}\mathbf{x}(n) + \boldsymbol{\eta}(n), \tag{3.23}$$

where

$$\mathbf{H} = \begin{bmatrix} h(0) & h(1) & \cdots & h(L_{\mathrm{h}}-1) & 0 & \cdots & 0 \\ 0 & h(0) & h(1) & \cdots & h(L_{\mathrm{h}}-1) & 0 & \vdots \\ \vdots & & \ddots & & \ddots & & \vdots \\ 0 & \cdots & 0 & h(0) & h(1) & \cdots & h(L_{\mathrm{h}}-1) \end{bmatrix} \tag{3.24}$$

and $\boldsymbol{\eta}(n)$ is a vector of gaussian noise. We can represent the feedback decision points $\hat{\mathbf{d}}(n)$ to the transmitted signal by the following:

$$\hat{\mathbf{d}}(n) = \mathbf{x}(n - \Delta), \tag{3.25}$$

where $\Delta$ is the sample delay between the equalizer solution and the actual transmitted symbol. The total data used in the equalizer from the received signal and the decision feedback can be shown as

$$\mathbf{y}(n) = \begin{bmatrix} \mathbf{z}_d(n) \\ \hline \hat{\mathbf{d}}(n) \end{bmatrix} = \left[\begin{array}{c} \mathbf{H} \\ \hline \mathbf{0\ P\ 0} \end{array}\right] \mathbf{x}(n) + \boldsymbol{\eta}(n), \tag{3.26}$$

where $\mathbf{P}$ is a $L_{\mathrm{FB}}$ x $L_{\mathrm{FB}}$ matrix of the form

$$\mathbf{P} = \begin{bmatrix} -1 & 0 & 0 & \cdots & 0 \\ 0 & -j & 0 & \cdots & 0 \\ 0 & 0 & -1 & \ddots & \vdots \\ \vdots & \vdots & \ddots & \ddots & 0 \\ 0 & 0 & \cdots & 0 & -j \end{bmatrix}. \tag{3.27}$$

The number of columns of zeros to the left and right of the $\mathbf{P}$ matrix is dependent on the sample delay $\Delta$. To facilitate the examination of the real and imaginary components of the equalizer output, we must also separate the receive signal and filter taps into their orthogonal components. For clarity in the derivation, let us assume at time $n$ that $x(n)$ is real and $\Delta$ is an even value such that $x(n-\Delta)$ is also real. Also, we will use the subscripts R and I to denote the real and imaginary part of the variable, respectively. (3.26) can be expressed as

$$\mathbf{y}_{\mathrm{R}} = \mathbf{H}_1\mathbf{x} + \boldsymbol{\eta}_{\mathrm{R}} \tag{3.28}$$

$$\mathbf{y}_{\mathrm{I}} = \mathbf{H}_2\mathbf{x} + \boldsymbol{\eta}_{\mathrm{I}}, \tag{3.29}$$

where $\mathbf{x}$ is previously defined, $\boldsymbol{\eta}_{\mathrm{R}}$ and $\boldsymbol{\eta}_{\mathrm{I}}$ are the real and imaginary components of the complex gaussian noise $\boldsymbol{\eta}$,

$$\mathbf{y}_{\mathrm{R}} = \begin{bmatrix} \mathbf{z}_{d,\mathrm{R}}(n) \\ \hat{\mathbf{d}}_{\mathrm{R}}(n) \end{bmatrix} \tag{3.30}$$

$$\mathbf{y}_{\mathrm{I}} = \begin{bmatrix} \mathbf{z}_{d,\mathrm{I}}(n) \\ \hat{\mathbf{d}}_{\mathrm{I}}(n) \end{bmatrix} \tag{3.31}$$

$$\mathbf{H}_1 = \begin{bmatrix} h_{\mathrm{R}}(0) & -h_{\mathrm{I}}(1) & \cdots & -h_{\mathrm{I}}(L_{\mathrm{h}}-1) & 0 & \cdots & 0 \\ 0 & -h_{\mathrm{I}}(0) & h_{\mathrm{R}}(1) & \cdots & h_{\mathrm{R}}(L_{\mathrm{h}}-1) & \ddots & \vdots \\ \vdots & \ddots & & \ddots & & \ddots & 0 \\ 0 & \cdots & 0 & -h_{\mathrm{I}}(0) & h_{\mathrm{R}}(1) & \cdots & h_{\mathrm{R}}(L_{\mathrm{h}}-1) \\ 0 & 0 & -1 & 0 & 0 & \cdots & 0 \\ 0 & 0 & 0 & 0 & \ddots & & \vdots \\ \vdots & \ddots & & \ddots & & \ddots & \vdots \\ \vdots & & \ddots & 0 & -1 & 0 & 0 \\ 0 & \cdots & \cdots & 0 & 0 & 0 & 0 \end{bmatrix} \tag{3.32}$$

$$\mathbf{H}_2 = \begin{bmatrix} h_{\mathrm{I}}(0) & h_{\mathrm{R}}(1) & \cdots & h_{\mathrm{R}}(L_{\mathrm{h}}-1) & 0 & \cdots & 0 \\ 0 & h_{\mathrm{R}}(0) & h_{\mathrm{I}}(1) & \cdots & h_{\mathrm{I}}(L_{\mathrm{h}}-1) & \ddots & \vdots \\ \vdots & \ddots & & \ddots & & \ddots & \vdots \\ 0 & \cdots & 0 & h_{\mathrm{R}}(0) & h_{\mathrm{I}}(1) & \cdots & h_{\mathrm{I}}(L_{\mathrm{h}}-1) \\ 0 & 0 & 0 & 0 & 0 & \cdots & 0 \\ 0 & 0 & 0 & -1 & \ddots & & \vdots \\ \vdots & \ddots & & \ddots & & \ddots & \vdots \\ \vdots & & \ddots & 0 & 0 & 0 & 0 \\ 0 & \cdots & \cdots & 0 & 0 & -1 & 0 \end{bmatrix}. \tag{3.33}$$

The complex equalizer output can be separated into its real and imaginary components as follows:

$$\begin{aligned} z(n) &= \mathbf{w}_{\mathrm{FF}}^T \mathbf{z}_d + \mathbf{w}_{\mathrm{FB}}^T \hat{\mathbf{d}} \\ &= (\mathbf{w}_{\mathrm{FF,R}}^T + j\mathbf{w}_{\mathrm{FF,I}}^T)(\mathbf{z}_{d,\mathrm{R}} + j\mathbf{z}_{d,\mathrm{I}}) + (\mathbf{w}_{\mathrm{FB,R}}^T + j\mathbf{w}_{\mathrm{FB,I}}^T)(\hat{\mathbf{d}}_{\mathrm{R}} + j\hat{\mathbf{d}}_{\mathrm{I}}) \\ &= (\mathbf{w}_{\mathrm{FF,R}}^T \mathbf{z}_{d,\mathrm{R}} - \mathbf{w}_{\mathrm{FF,I}}^T \mathbf{z}_{d,\mathrm{I}}) + j(\mathbf{w}_{\mathrm{FF,R}}^T \mathbf{z}_{d,\mathrm{I}} + \mathbf{w}_{\mathrm{FF,I}}^T \mathbf{z}_{d,\mathrm{R}}) \\ &\quad + (\mathbf{w}_{\mathrm{FB,R}}^T \hat{\mathbf{d}}_{\mathrm{R}} - \mathbf{w}_{\mathrm{FB,I}}^T \hat{\mathbf{d}}_{\mathrm{I}}) + j(\mathbf{w}_{\mathrm{FB,R}}^T \hat{\mathbf{d}}_{\mathrm{I}} + \mathbf{w}_{\mathrm{FB,I}}^T \hat{\mathbf{d}}_{\mathrm{R}}). \end{aligned} \tag{3.34}$$

For the assumptions previously stated, only the real part of the equalizer output is needed at time $n$. Choosing the real part of the equalizer output and rearranging the variables, the real component of (3.34) becomes

$$\Re\{z(n)\} = (\mathbf{w}_{\mathrm{FF,R}}^T \mathbf{z}_{d,\mathrm{R}} + \mathbf{w}_{\mathrm{FB,R}}^T \hat{\mathbf{d}}_{\mathrm{R}}) - (\mathbf{w}_{\mathrm{FF,I}}^T \mathbf{z}_{d,\mathrm{I}} + \mathbf{w}_{\mathrm{FB,I}}^T \hat{\mathbf{d}}_{\mathrm{I}}). \tag{3.35}$$

Using the terms in (3.30) and (3.31), the real part of $z(n)$ can then be rewritten as

$$\Re\{z(n)\} = \hat{\mathbf{w}}_{\mathrm{R}}\mathbf{y}_{\mathrm{R}} - \hat{\mathbf{w}}_{\mathrm{I}}\mathbf{y}_{\mathrm{I}}, \tag{3.36}$$

where

$$\hat{\mathbf{w}}_{\mathrm{R}} = \begin{bmatrix} \mathbf{w}_{\mathrm{FF,R}} \\ \mathbf{w}_{\mathrm{FB,R}} \end{bmatrix}^T \tag{3.37}$$

and

$$\hat{\mathbf{w}}_{\mathrm{I}} = \begin{bmatrix} \mathbf{w}_{\mathrm{FF,I}} \\ \mathbf{w}_{\mathrm{FB,I}} \end{bmatrix}^T . \tag{3.38}$$

The feedback filter taps are now concatenated with the feedforward filter taps. We now have all the necessary definitions to derive the minimum mean squared error for the DF-MMSE equalizer.

The error between the output of the the DF-MMSE equalizer at time $n$ and the transmitted symbol at $n - \Delta$ is

$$e(n) = \Re\{x(n-\Delta) - z(n)\} = x(n-\Delta) - \Re\{z(n)\}. \tag{3.39}$$

We can now substitute the variable definitions from the previous section into (3.39) to arrive at the following:

$$\begin{aligned} e(n) &= x(n-\Delta) - (\hat{\mathbf{w}}_{\mathrm{R}}\mathbf{y}_{\mathrm{R}} - \hat{\mathbf{w}}_{\mathrm{I}}\mathbf{y}_{\mathrm{I}}) \\ &= x(n-\Delta) - [\hat{\mathbf{w}}_{\mathrm{R}}(\mathbf{H}_1\mathbf{x} + \boldsymbol{\eta}_{\mathrm{R}}) - \hat{\mathbf{w}}_{\mathrm{I}}(\mathbf{H}_2\mathbf{x} + \boldsymbol{\eta}_{\mathrm{I}})] \\ &= x(n-\Delta) - [\hat{\mathbf{w}}_{\mathrm{R}}\mathbf{H}_1\mathbf{x} + \hat{\mathbf{w}}_{\mathrm{R}}\boldsymbol{\eta}_{\mathrm{R}} - \hat{\mathbf{w}}_{\mathrm{I}}\mathbf{H}_2\mathbf{x} - \hat{\mathbf{w}}_{\mathrm{I}}\boldsymbol{\eta}_{\mathrm{I}}] \\ &= x(n-\Delta) - \hat{\mathbf{w}}_{\mathrm{R}}\mathbf{H}_1\mathbf{x} - \hat{\mathbf{w}}_{\mathrm{R}}\boldsymbol{\eta}_{\mathrm{R}} + \hat{\mathbf{w}}_{\mathrm{I}}\mathbf{H}_2\mathbf{x} + \hat{\mathbf{w}}_{\mathrm{I}}\boldsymbol{\eta}_{\mathrm{I}}. \end{aligned} \tag{3.40}$$

The square of this error then becomes

$$\begin{aligned} e(n)e^*(n) &= |x(n-\Delta)|^2 - x(n-\Delta)\mathbf{x}^*\mathbf{H}_1^*\hat{\mathbf{w}}_{\mathrm{R}}^* - x(n-\Delta)\boldsymbol{\eta}_{\mathrm{R}}^*\hat{\mathbf{w}}_{\mathrm{R}}^* + x(n-\Delta)\mathbf{x}^*\mathbf{H}_2^*\hat{\mathbf{w}}_{\mathrm{I}}^* \\ &\quad + x(n-\Delta)\boldsymbol{\eta}_{\mathrm{I}}^*\hat{\mathbf{w}}_{\mathrm{I}}^* - \hat{\mathbf{w}}_R\mathbf{H}_1\mathbf{x}x(n-\Delta) + \hat{\mathbf{w}}_{\mathrm{R}}\mathbf{H}_1\mathbf{x}\mathbf{x}^*\mathbf{H}_1^*\hat{\mathbf{w}}_R^* + \hat{\mathbf{w}}_{\mathrm{R}}\mathbf{H}_1\mathbf{x}\boldsymbol{\eta}_{\mathrm{R}}^*\hat{\mathbf{w}}_R^* \\ &\quad - \hat{\mathbf{w}}_{\mathrm{R}}\mathbf{H}_1\mathbf{x}\mathbf{x}^*\mathbf{H}_2^*\hat{\mathbf{w}}_{\mathrm{I}}^* - \hat{\mathbf{w}}_{\mathrm{R}}\mathbf{H}_1\mathbf{x}\boldsymbol{\eta}_{\mathrm{I}}^*\hat{\mathbf{w}}_{\mathrm{I}}^* - \hat{\mathbf{w}}_{\mathrm{R}}\boldsymbol{\eta}_{\mathrm{R}}x(n-\Delta) + \hat{\mathbf{w}}_{\mathrm{R}}\boldsymbol{\eta}_{\mathrm{R}}\mathbf{x}^*\mathbf{H}_1^*\hat{\mathbf{w}}_{\mathrm{I}}^* \\ &\quad + \hat{\mathbf{w}}_{\mathrm{R}}\boldsymbol{\eta}_{\mathrm{R}}\boldsymbol{\eta}_{\mathrm{R}}^*\hat{\mathbf{w}}_{\mathrm{R}}^* - \hat{\mathbf{w}}_{\mathrm{R}}\boldsymbol{\eta}_{\mathrm{R}}\mathbf{x}^*\mathbf{H}_2^*\hat{\mathbf{w}}_{\mathrm{I}}^* - \hat{\mathbf{w}}_{\mathrm{R}}\boldsymbol{\eta}_{\mathrm{R}}\boldsymbol{\eta}_{\mathrm{I}}^*\hat{\mathbf{w}}_{\mathrm{I}}^* + \hat{\mathbf{w}}_{\mathrm{I}}\mathbf{H}_2\mathbf{x}x(n-\Delta) \\ &\quad - \hat{\mathbf{w}}_{\mathrm{I}}\mathbf{H}_2\mathbf{x}\mathbf{x}^*\mathbf{H}_1^*\hat{\mathbf{w}}_{\mathrm{R}}^* - \hat{\mathbf{w}}_{\mathrm{I}}\mathbf{H}_2\mathbf{x}\boldsymbol{\eta}_{\mathrm{R}}^*\hat{\mathbf{w}}_{\mathrm{R}}^* + \hat{\mathbf{w}}_{\mathrm{I}}\mathbf{H}_2\mathbf{x}\mathbf{x}^*\mathbf{H}_2^*\hat{\mathbf{w}}_{\mathrm{I}}^* + \hat{\mathbf{w}}_{\mathrm{I}}H_2\mathbf{x}\boldsymbol{\eta}_{\mathrm{I}}^*\hat{\mathbf{w}}_{\mathrm{I}}^* + \\ &\quad + \hat{\mathbf{w}}_{\mathrm{I}}\boldsymbol{\eta}_{\mathrm{I}}x(n-\Delta) - \hat{\mathbf{w}}_{\mathrm{I}}\boldsymbol{\eta}_{\mathrm{I}}\mathbf{x}^*\mathbf{H}_1^*\hat{\mathbf{w}}_{\mathrm{R}}^* - \hat{\mathbf{w}}_{\mathrm{I}}\boldsymbol{\eta}_{\mathrm{I}}\boldsymbol{\eta}_{\mathrm{R}}^*\hat{\mathbf{w}}_{\mathrm{R}}^* + \hat{\mathbf{w}}_{\mathrm{I}}\boldsymbol{\eta}_{\mathrm{I}}\mathbf{x}^*\mathbf{H}_2^*\hat{\mathbf{w}}_{\mathrm{I}}^* \\ &\quad + \hat{\mathbf{w}}_{\mathrm{I}}\boldsymbol{\eta}_{\mathrm{I}}\boldsymbol{\eta}_{\mathrm{I}}^*\hat{\mathbf{w}}_{\mathrm{I}}^*. \end{aligned} \tag{3.41}$$

Assuming that the received noise has zero mean and is uncorrelated with the input data, the expectation of the squared error becomes

$$\begin{aligned} E[e(n)e^*(n)] &= |x(n-\Delta)|^2 - \boldsymbol{\delta}^*\mathbf{H}_1^*\hat{\mathbf{w}}_{\mathrm{R}}^* + \boldsymbol{\delta}^*\mathbf{H}_2^*\hat{\mathbf{w}}_{\mathrm{I}}^* - \hat{\mathbf{w}}_{\mathrm{R}}\mathbf{H}_1\boldsymbol{\delta} \\ &\quad + \hat{\mathbf{w}}_{\mathrm{R}}[\mathbf{H}_1\mathbf{H}_1^* + E(\boldsymbol{\eta}_{\mathrm{R}}\boldsymbol{\eta}_{\mathrm{R}}^*)]\hat{\mathbf{w}}_{\mathrm{R}}^* - \hat{\mathbf{w}}_{\mathrm{R}}\mathbf{H}_1\mathbf{H}_2^*\hat{\mathbf{w}}_{\mathrm{I}}^* \\ &\quad + \hat{\mathbf{w}}_{\mathrm{I}}\mathbf{H}_2\boldsymbol{\delta} - \hat{\mathbf{w}}_{\mathrm{I}}\mathbf{H}_2\mathbf{H}_1^*\hat{\mathbf{w}}_{\mathrm{R}}^* + \hat{\mathbf{w}}_{\mathrm{I}}[\mathbf{H}_2\mathbf{H}_2^* + E(\boldsymbol{\eta}_{\mathrm{I}}\boldsymbol{\eta}_{\mathrm{I}}^*)]\hat{\mathbf{w}}_{\mathrm{I}}^*, \quad (3.42) \end{aligned}$$

where $\boldsymbol{\delta}$ is a column vector with $|x(n-\Delta)|^2$ on the $\Delta$-th row:

$$\boldsymbol{\delta} = [\ 0\ \cdots\ 0\ |x(n-\Delta)|^2\ 0\ \cdots\ 0\ ]^T. \quad (3.43)$$

The expectation of the squared error (3.42) is substituted into (3.20) in order to find a minimized solution for $J$. The gradient of $J$ is taken with respect to $\hat{\mathbf{w}}_{\mathrm{R}}$ and $\hat{\mathbf{w}}_{\mathrm{I}}$ and is set to zero as shown:

$$\nabla_{\hat{\mathbf{w}}_{\mathrm{R}}} J = 0 \quad (3.44)$$

$$\nabla_{\hat{\mathbf{w}}_{\mathrm{I}}} J = 0. \quad (3.45)$$

Solving these two equations lead to the following expressions:

$$\mathbf{H}_1\boldsymbol{\delta} = [\mathbf{H}_1\mathbf{H}_1^* + E(\boldsymbol{\eta}_{\mathrm{R}}\boldsymbol{\eta}_{\mathrm{R}}^*)]\hat{\mathbf{w}}_{\mathrm{R}}^* - \mathbf{H}_1\mathbf{H}_2^*\hat{\mathbf{w}}_{\mathrm{I}}^* \quad (3.46)$$

$$-\mathbf{H}_2\boldsymbol{\delta} = -\mathbf{H}_2\mathbf{H}_1^*\hat{\mathbf{w}}_{\mathrm{R}}^* + [\mathbf{H}_2\mathbf{H}_2^* + E(\boldsymbol{\eta}_{\mathrm{I}}\boldsymbol{\eta}_{\mathrm{I}}^*)]\hat{\mathbf{w}}_{\mathrm{I}}^*. \quad (3.47)$$

If we define the following for compactness:

$$\mathbf{p} = \begin{bmatrix} \mathbf{H}_1\boldsymbol{\delta} \\ -\mathbf{H}_2\boldsymbol{\delta} \end{bmatrix} \quad (3.48)$$

$$\hat{\mathbf{w}}^* = \begin{bmatrix} \hat{\mathbf{w}}_{\mathrm{R}}^* \\ \hat{\mathbf{w}}_{\mathrm{I}}^* \end{bmatrix} \quad (3.49)$$

$$\mathbf{R} = \begin{bmatrix} \mathbf{H}_1\mathbf{H}_1^* + E(\boldsymbol{\eta}_{\mathrm{R}}\boldsymbol{\eta}_{\mathrm{R}}^*) & -\mathbf{H}_1\mathbf{H}_2^* \\ -\mathbf{H}_2\mathbf{H}_1^* & \mathbf{H}_2\mathbf{H}_2^* + E(\boldsymbol{\eta}_{\mathrm{I}}\boldsymbol{\eta}_{\mathrm{I}}^*) \end{bmatrix}, \quad (3.50)$$

then (3.46) and (3.47) can be represented as

$$\mathbf{p} = \mathbf{R}\hat{\mathbf{w}}^* \quad (3.51)$$

and the optimal coefficients of the DF-MMSE equalizer can be written as

$$\hat{\mathbf{w}}^* = \mathbf{R}^{-1}\mathbf{p}. \quad (3.52)$$

**Iterative Solution**

Similar to the CMA derivation, the coefficients can be updated by a simple gradient search algorithm to minimize $J$ according to the following:

$$\mathbf{w}_{\mathrm{FF}}^{(n+1)} = \mathbf{w}_{\mathrm{FF}}^{(n)} - \mu \nabla_{\mathbf{w}_{\mathrm{FF}}} J \tag{3.53}$$

$$\mathbf{w}_{\mathrm{FB}}^{(n+1)} = \mathbf{w}_{\mathrm{FB}}^{(n)} - \mu \nabla_{\mathbf{w}_{\mathrm{FB}}} J. \tag{3.54}$$

Using (3.20), the gradient of $J$ with respect to the filter coefficients $\mathbf{w}_{\mathrm{FF}}$ and $\mathbf{w}_{\mathrm{FB}}$ is

$$\begin{aligned}
\nabla_{\mathbf{w}_{\mathrm{FF}}} J &= E\left[\Re\left\{\hat{d}(k) - z(n)\right\}\right] \nabla_{\mathbf{w}_{\mathrm{FF}}} \Re\left\{-z(n)\right\} \\
&= E\left[\Re\left\{\hat{d}(k) - z(n)\right\}\right] \nabla_{\mathbf{w}_{\mathrm{FF}}} \Re\left\{-\mathbf{w}_{\mathrm{FF}}^T \mathbf{z}_d(n) - \mathbf{w}_{\mathrm{FB}}^T \mathbf{d}(n)\right\} \\
&= E\left[\Re\left\{\hat{d}(k) - z(n)\right\}\right] \nabla_{\mathbf{w}_{\mathrm{FF}}} \Re\left\{-\mathbf{w}_{\mathrm{FF}}^T \mathbf{z}_d(n)\right\} \\
&= E\left[\Re\left\{\hat{d}(k) - z(n)\right\}\right] \nabla_{\mathbf{w}_{\mathrm{FF}}} \left[-\Re\left\{\mathbf{w}_{\mathrm{FF}}^T\right\} \Re\left\{\mathbf{z}_d(n)\right\} + \Im\left\{\mathbf{w}_{\mathrm{FF}}^T\right\} \Im\left\{\mathbf{z}_d(n)\right\}\right] \\
&= E\left[\Re\left\{\hat{d}(k) - z(n)\right\}\right] \left[-\Re\left\{\mathbf{z}_d(n)\right\} + j\Im\left\{\mathbf{z}_d(n)\right\}\right] \\
&= E\left[\Re\left\{\hat{d}(k) - z(n)\right\}\right] \left[-\mathbf{z}_d^*(n)\right]
\end{aligned} \tag{3.55}$$

$$\begin{aligned}
\nabla_{\mathbf{w}_{\mathrm{FB}}} J &= E\left[\Re\left\{\hat{d}(k) - z(n)\right\}\right] \nabla_{\mathbf{w}_{\mathrm{FB}}} \Re\left\{-z(n)\right\} \\
&= E\left[\Re\left\{\hat{d}(k) - z(n)\right\}\right] \nabla_{\mathbf{w}_{\mathrm{FB}}} \Re\left\{-\mathbf{w}_{\mathrm{FF}}^T \mathbf{z}_d(n) - \mathbf{w}_{\mathrm{FB}}^T \mathbf{d}(n)\right\} \\
&= E\left[\Re\left\{\hat{d}(k) - z(n)\right\}\right] \nabla_{\mathbf{w}_{\mathrm{FB}}} \Re\left\{-\mathbf{w}_{\mathrm{FB}}^T \mathbf{d}(n)\right\} \\
&= E\left[\Re\left\{\hat{d}(k) - z(n)\right\}\right] \nabla_{\mathbf{w}_{\mathrm{FB}}} \left[-\Re\left\{\mathbf{w}_{\mathrm{FB}}^T\right\} \Re\left\{\mathbf{d}(n)\right\} + \Im\left\{\mathbf{w}_{\mathrm{FB}}^T\right\} \Im\left\{\mathbf{d}(n)\right\}\right] \\
&= E\left[\Re\left\{\hat{d}(k) - z(n)\right\}\right] \left[-\Re\left\{\mathbf{d}(n)\right\} + j\Im\left\{\mathbf{d}(n)\right\}\right] \\
&= E\left[\Re\left\{\hat{d}(k) - z(n)\right\}\right] \left[-\mathbf{d}^*(n)\right].
\end{aligned} \tag{3.56}$$

The adaptive algorithm is obtained by replacing the true gradient of (3.55) and (3.56) with an instantaneous gradient estimate, or one point average, given as

$$\hat{\nabla}_{\mathbf{w}_{\mathrm{FF}}} J = \left[\Re\left\{\hat{d}(k) - z(n)\right\}\right] \left[-\mathbf{z}_d^*(n)\right] \tag{3.57}$$

$$\hat{\nabla}_{\mathbf{w}_{\mathrm{FB}}} J = \left[\Re\left\{\hat{d}(k) - z(n)\right\}\right] \left[-\mathbf{d}^*(n)\right]. \tag{3.58}$$

Substituting the instantaneous gradient estimates into (3.53) and (3.54) yield the desired algorithm

$$\mathbf{w}_{\mathrm{FF}}^{(n+1)} = \mathbf{w}_{\mathrm{FF}}^{(n)} + \mu e(n) \mathbf{z}_d^*(n) \tag{3.59}$$

$$\mathbf{w}_{\mathrm{FB}}^{(n+1)} = \mathbf{w}_{\mathrm{FB}}^{(n)} + \mu e(n)\mathbf{d}^*(n), \tag{3.60}$$

where the error term $e(n)$ is defined to be

$$e(n) = \left[\Re\left\{\hat{d}(k) - z(n)\right\}\right]. \tag{3.61}$$

A similar derivation to minimize error along the imaginary component for $n$ odd produces the same filter updates given by (3.59) and (3.60) but with the error term $e(n)$ defined as

$$e(n) = \left[j\Im\left\{\hat{d}(k) - z(n)\right\}\right]. \tag{3.62}$$

Figure 3.4 shows the new block diagram of the symbol detector and DF-MMSE equalizer with filter tap updates realized by (3.59) and (3.60).

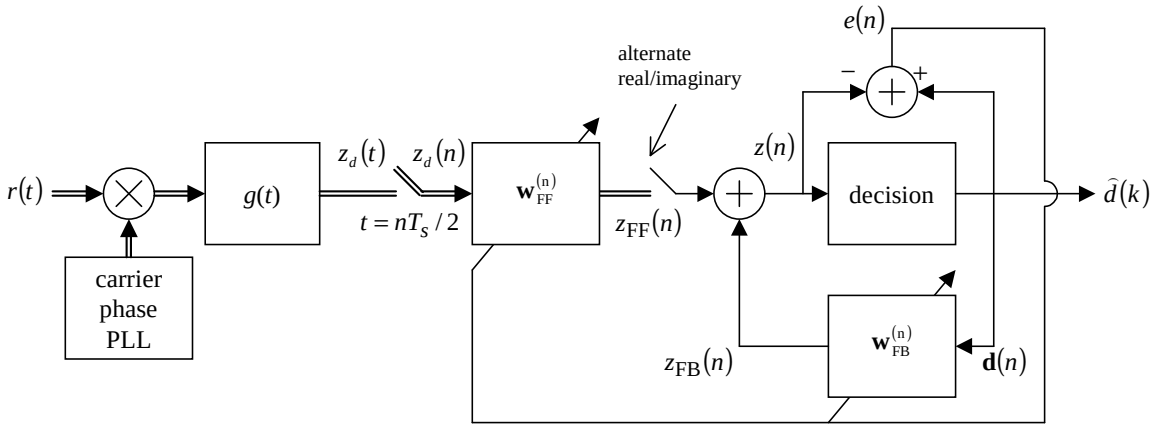


Figure 3.4: Symbol-by-symbol detector with DF-MMSE equalizer showing the filter tap update according to (3.59) and (3.60).

# Chapter 4

# Performance

This chapter outlines the test procedures for the DF-MMSE and CMA equalizers to determine their effectiveness in mitigating multipath distortion encountered on the aeronautical telemetry channels. Mean-Squared Error (MSE) and Bit Error Rate (BER) measurements were taken for various signal-to-noise ratios, and compared to the unequalized transmissions of the ARTM Tier-1 waveforms (SOQPSK-TG and FQPSK). The results of these measurements are discussed at the end of this chapter.

## 4.1 Test Procedure

The performance of both FQPSK and SOQPSK-TG using both the CMA and the DF-MMSE equalizers were simulated in the presence of multipath interference typical of that encountered in aeronautical telemetry [8] as described in Chapter 2. In the simulations, the channel impulse response is

$$h(t) = \delta(t) + |\Gamma_1| e^{j\pi} \delta\left(t - 0.5T_s\right). \tag{4.1}$$

The phase of $\Gamma_1$ is set to $\pi$ to produce the worst-case multipath interference. $|\Gamma_1|$ was varied from 0.1 to 0.8 to monitor the effect of the relative strength of the multipath interference. The simulations with the DF-MMSE equalizer used the following parameters:

- $N = 2$ samples/symbol
- $L_{\mathrm{FF}} = 21, L_{\mathrm{FB}} = 18$ (at 2 samples/symbol, the filters spanned 19.5 symbols or 39 bits)

- Training length = 3000 bits
- LMS step size $\mu = 10^{-3}$

The simulations using the CMA equalizer used the following parameters:

- $N = 10$ samples/symbol
- $L = 195$ (the filter spans 19.5 symbols or 39 bits)
- Filter tap initialization period = 3000 bits
- LMS step size $\mu = 10^{-5}$

MSE measurements were recorded after the detection filter output $d(k)$ for the CMA implementation as shown in Figure 3.2. For the test with the DF-MMSE equalizer, the MSE measurements were recorded at the equalizer output $z(n)$ shown in Figure 3.4.

## 4.2 MSE Results

The simulation results for FQPSK are shown in Figures 4.1, 4.2, and 4.3. Figure 4.1 is a plot of the mean-squared error performance of unequalized FQPSK and is included for reference. A comparison of the mean-squared error for FQPSK using CMA equalization (Figure 4.2) and DF-MMSE equalization (Figure 4.3) shows that the DF-MMSE equalizer performs better than the CMA equalizer. This is expected since the criteria for the DF-MMSE equalizer is to minimize the mean-squared error at the point of measurement, whereas the CMA equalizer will only, at best, attempt to match the inherent MSE of an unequalized FQPSK in a non-multipath environment. Also note that for the lower values of $E_b/N_0$, the MSE of the CMA equalizer is larger than the MSE of an unequalized FQPSK, especially as $|\Gamma_1|$ increases, but the MSE of the CMA equalizer shows considerable improvement over the unequalized FQPSK for larger values of $E_b/N_0$. However, the higher MSE values from the CMA equalizer at low $E_b/N_0$ does not decrease the BER performance compared to the unequalized FQPSK, as the results show in the next section.

The simulation results for SOQPSK-TG are shown in Figures 4.4, 4.5, and 4.6. Figure 4.4 is a plot of the mean-squared error performance of unequalized SOQPSK-TG and is included for reference. A comparison of the mean-squared error for SOQPSK-TG using CMA equalization (Figure 4.5) and DF-MMSE equalization (Figure 4.6) shows again that the DF-MMSE equalizer has a lower MSE compared to that of the CMA equalizer.

## 4.3 BER Results

The simulation results for FQPSK are shown in Figures 4.7, 4.8, and 4.9. Figure 4.7 is a plot of the bit error rate performance of unequalized FQPSK and is included for reference. A comparison of the bit error rate for FQPSK using CMA equalization (Figure 4.8) and DF-MMSE equalization (Figure 4.9) shows that the DF-MMSE equalizer seems to perform a little better than the CMA equalizer, which is due to the DF-MMSE equalizer having a lower MSE than the CMA equalizer, although both improve the bit error rate performance. The performance improvement is more pronounced as $|\Gamma_1|$ increases.

The simulation results for SOQPSK-TG are shown in Figures 4.10, 4.11, and 4.12. Figure 4.10 is a plot of the bit error rate performance of unequalized SOQPSK-TG and is included for reference. A comparison of the bit error rate for SOQPSK-TG using CMA equalization (Figure 4.11) and DF-MMSE equalization (Figure 4.12) shows that the DF-MMSE equalizer seems to perform a little better than the CMA equalizer, similar to the characteristic observed for FQPSK.

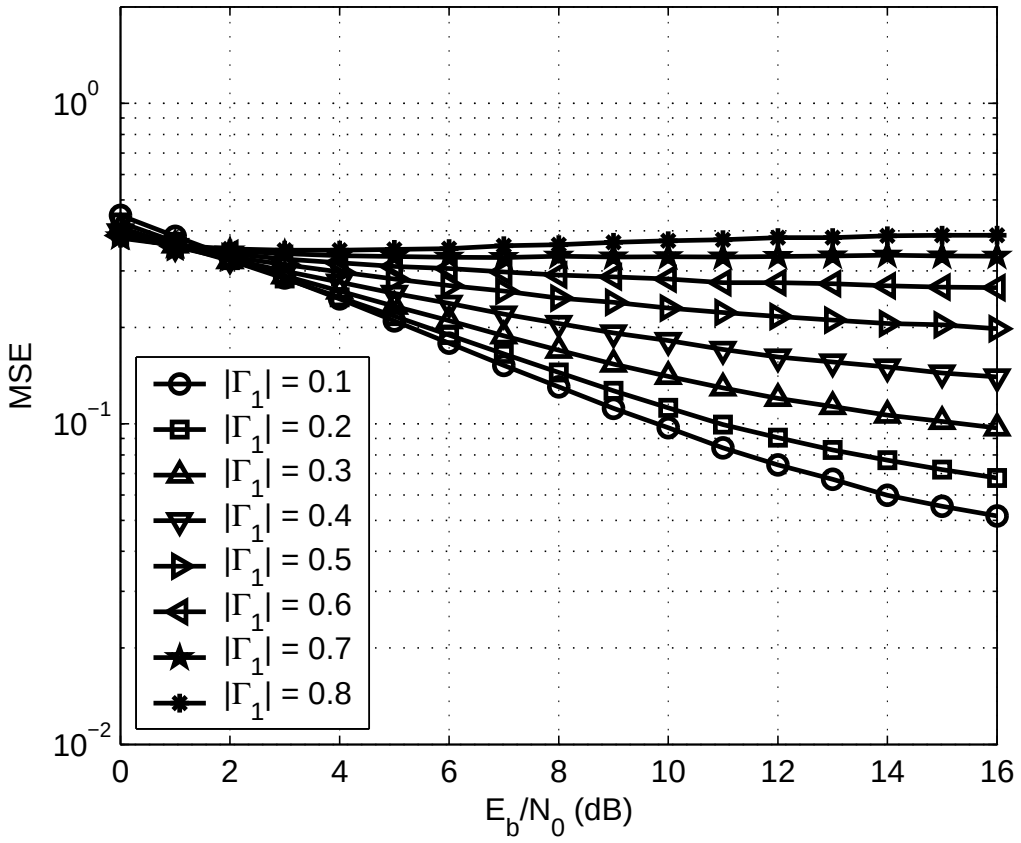


Figure 4.1: MSE performance of unequalized FQPSK on the channel (4.1).

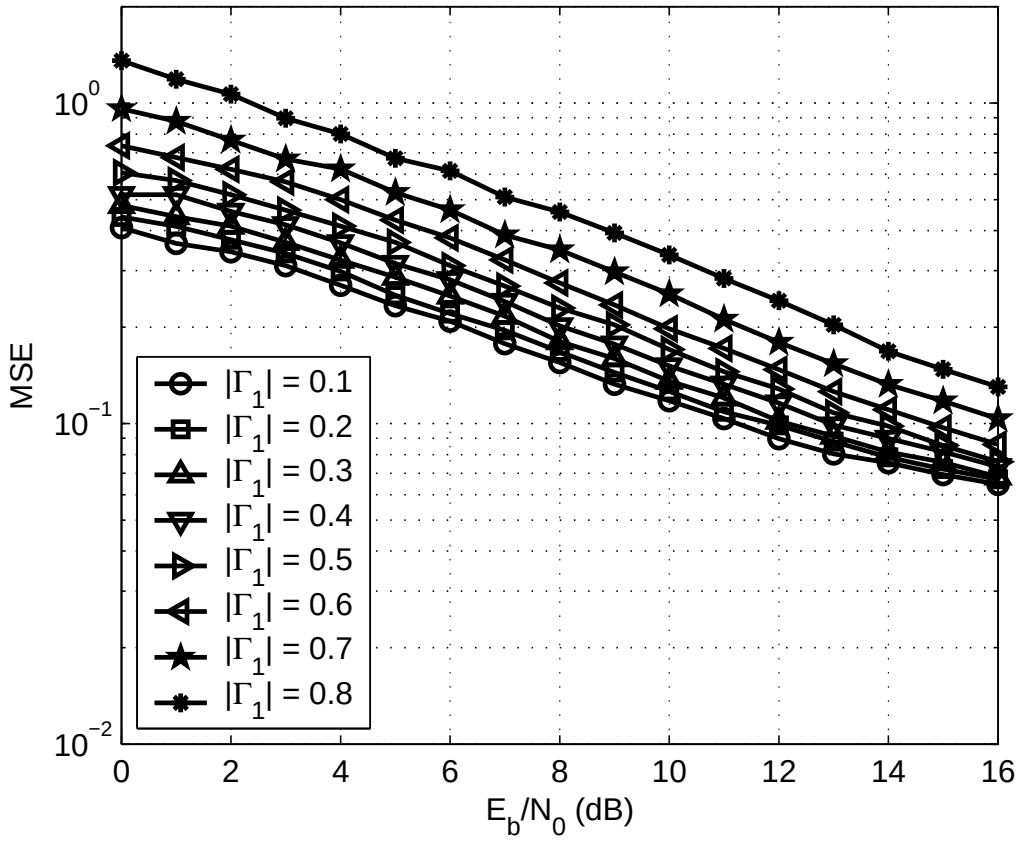


Figure 4.2: MSE performance of FQPSK using the CMA equalizer on the channel (4.1).

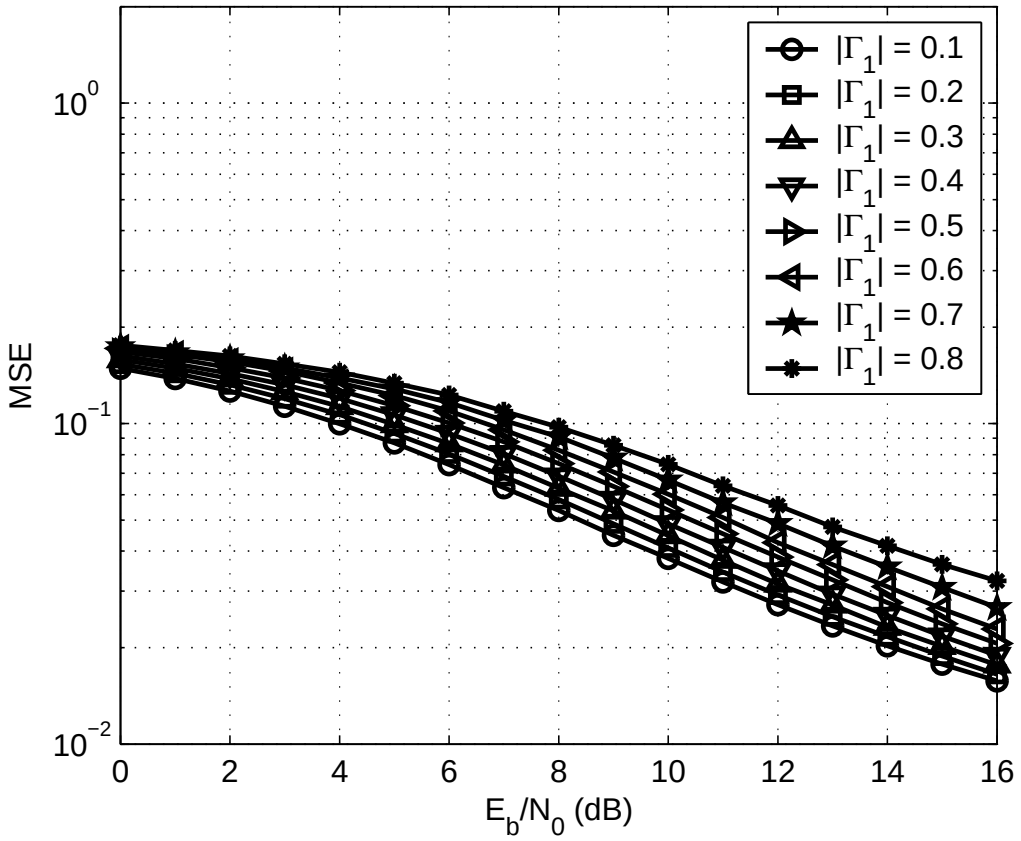


Figure 4.3: MSE performance of FQPSK using the DF-MMSE equalizer on the channel (4.1).

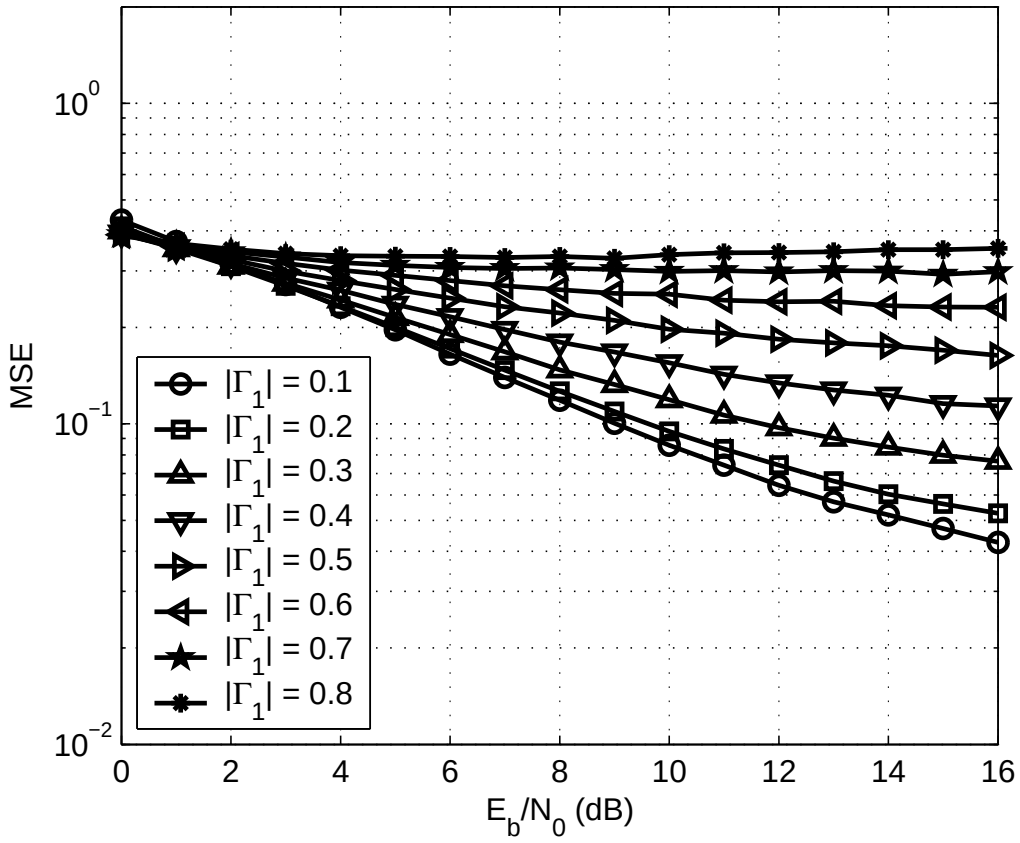


Figure 4.4: MSE performance of unequalized SOQPSK-TG on the channel (4.1).

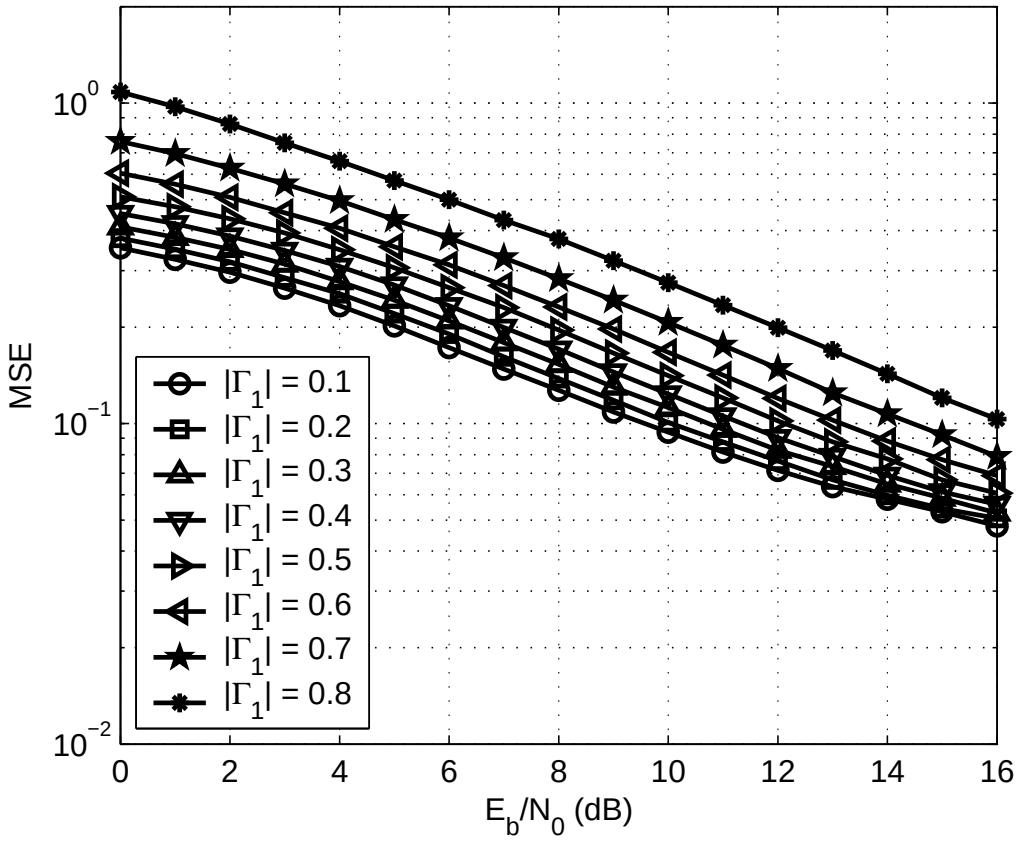


Figure 4.5: MSE performance of SOQPSK-TG using the CMA equalizer on the channel (4.1).

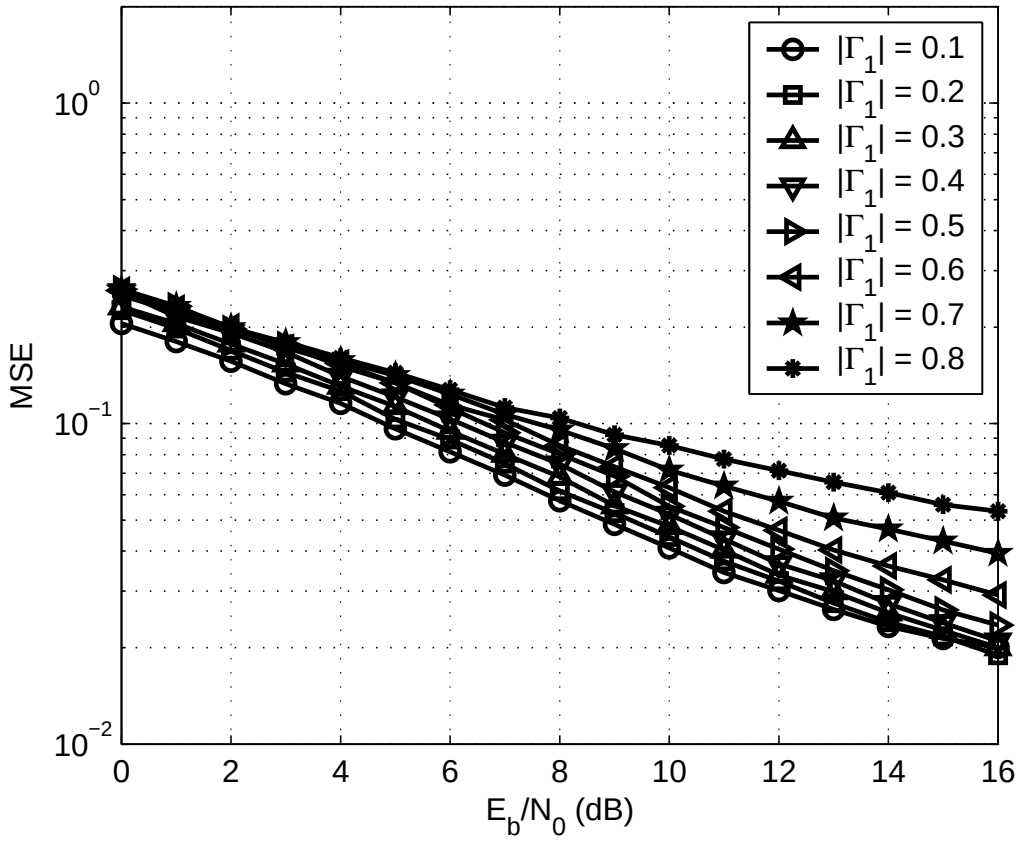


Figure 4.6: MSE performance of SOQPSK-TG using the DF-MMSE equalizer on the channel (4.1).

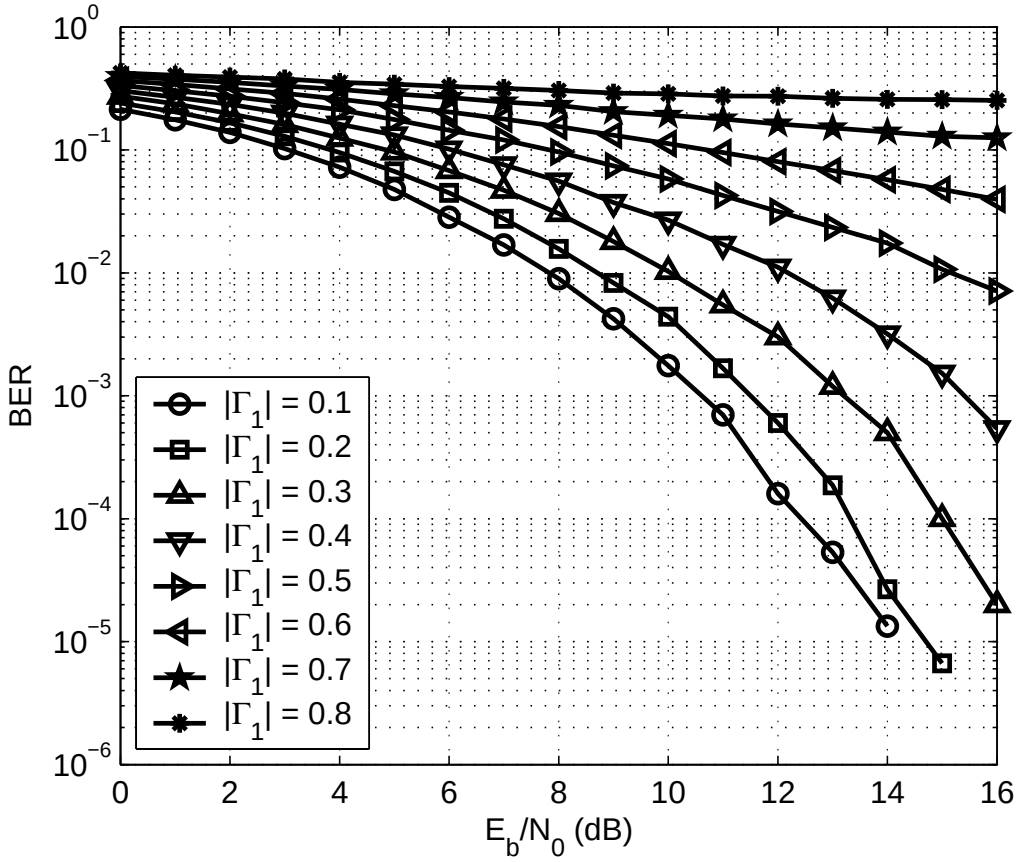


Figure 4.7: BER performance of unequalized FQPSK on the channel (4.1).

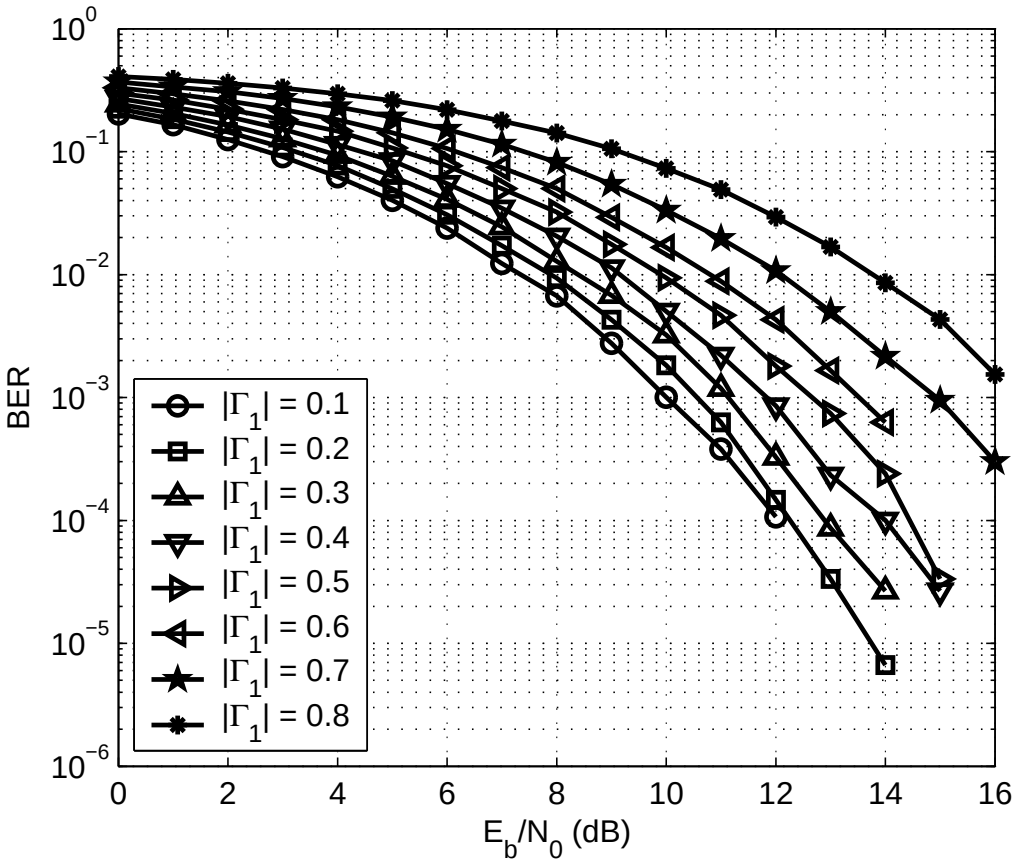


Figure 4.8: BER performance of FQPSK using the CMA equalizer on the channel (4.1).

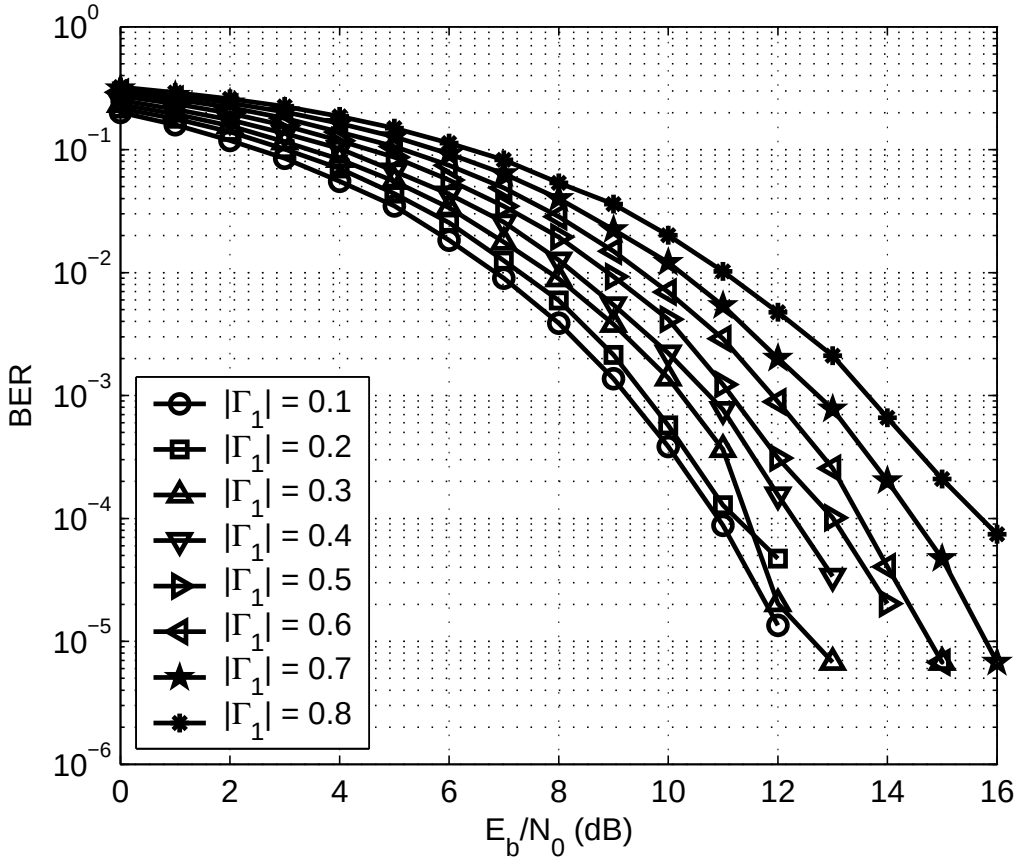


Figure 4.9: BER performance of FQPSK using the DF-MMSE equalizer on the channel (4.1).

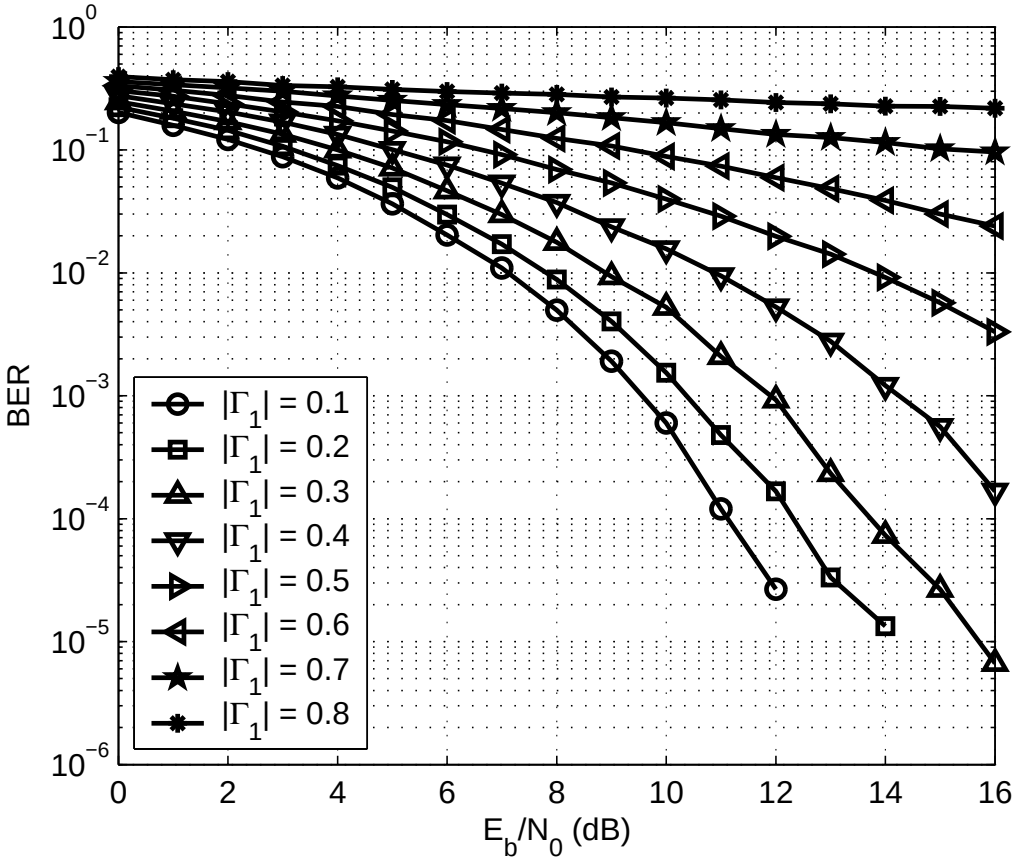


Figure 4.10: BER performance of unequalized SOQPSK-TG on the channel (4.1).

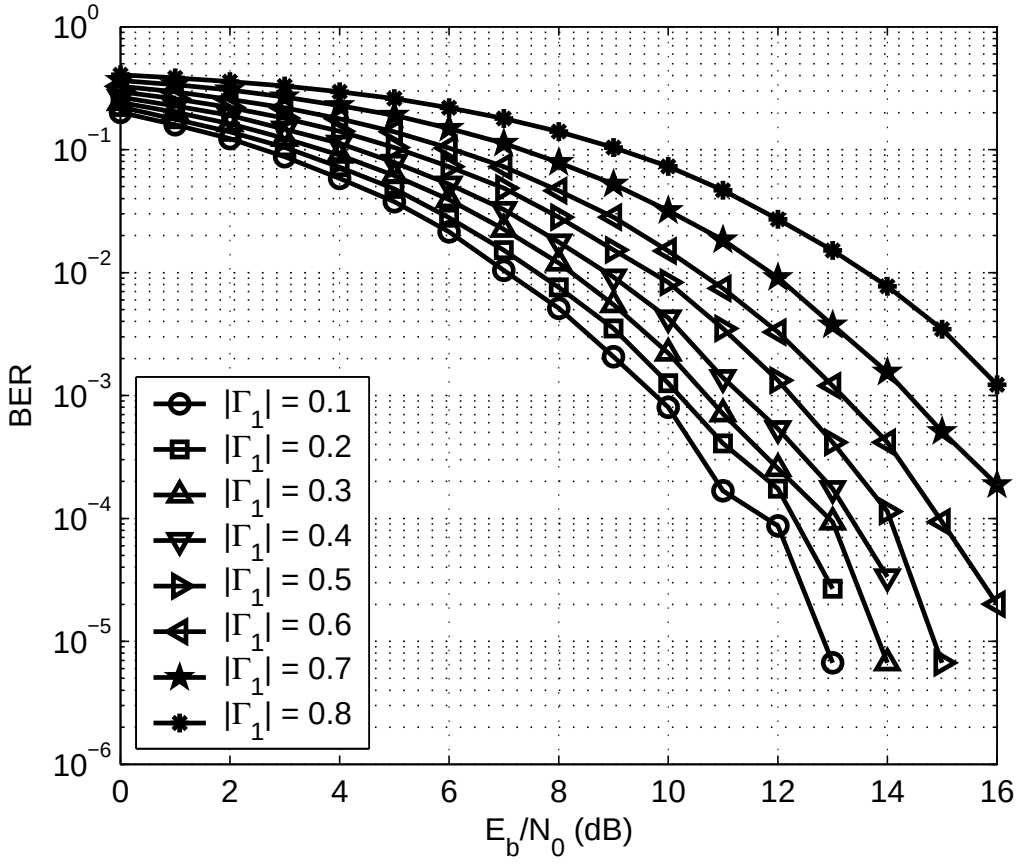


Figure 4.11: BER performance of SOQPSK-TG using the CMA equalizer on the channel (4.1).

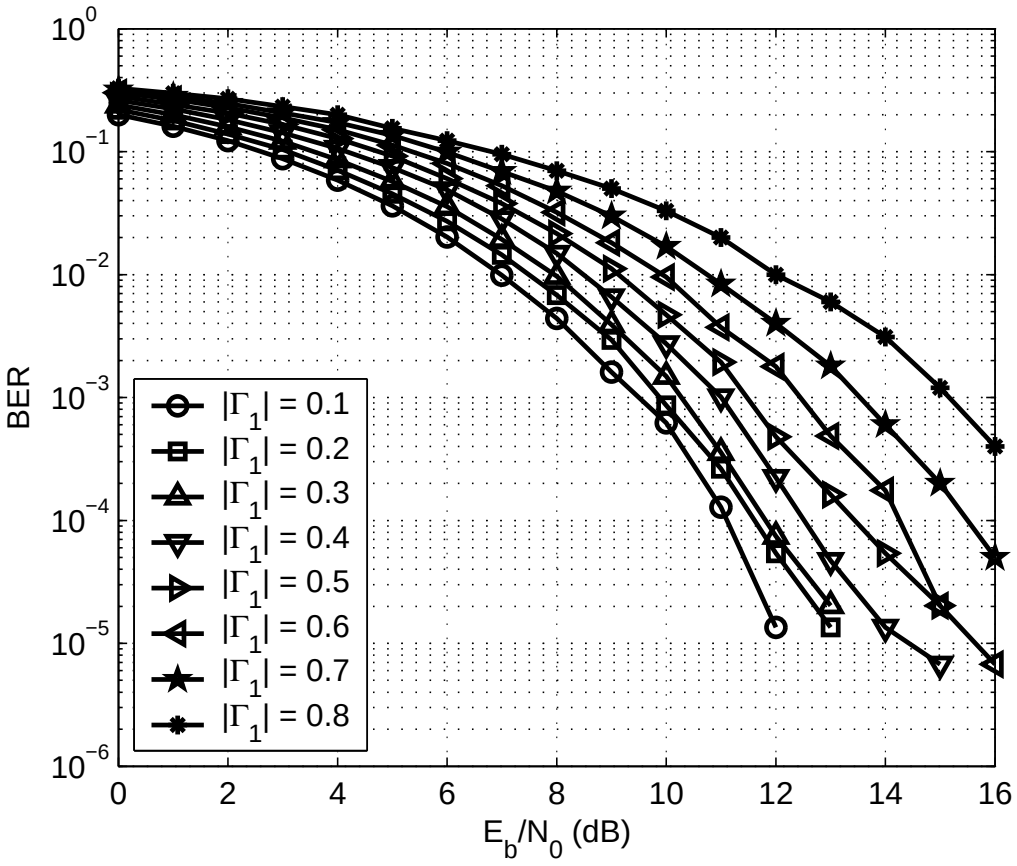


Figure 4.12: BER performance of SOQPSK-TG using the DF-MMSE equalizer on the channel (4.1).

# Chapter 5

# Conclusion

While both CMA and DF-MMSE equalizers are able to reduce the performance loss due to multipath interference to acceptable levels, there are implementation differences that should be noted. Both equalizers were chosen to span the same number of bit intervals. Since the DF-MMSE equalizer operates at two samples/symbol, it requires fewer multiplies than the CMA equalizer. The number of CMA filter coefficients would be the same as the number of filter coefficients for the DF-MMSE equalizer if the CMA equalizer could operate at two samples/symbol. However simulation results show significant performance degradations when the detection filter operates at 2 samples/symbol. These same results suggest $N = 10$ samples/symbol produces nearly optimum results. Thus, for the ARTM Tier-1 waveforms, the CMA equalizer will require more filter coefficients than the DF-MMSE equalizer.

The CMA equalizer is truly blind; it does not require knowledge of the data symbols, carrier phase, or timing synchronization to operate. This is an attractive feature since multipath interference often makes it difficult to obtain accurate estimates of the carrier phase and symbol timing. The DF-MMSE requires a known training sequence, at least from a "cold start." Simulation results with carrier phase offset also show that the DF-MMSE equalizer requires at least course carrier phase synchronization to achieve acceptable performance. Normally, DF-MMSE equalizers also require symbol timing and it is common knowledge that fractionally spaced equalizers are less susceptible to symbol timing errors than symbol-spaced equalizers [9]. However, if the feedforward filter is long enough, the DF-MMSE equalizer is still able to function. The feedforward filter adapts to a filter that compensates for

the multipath interference and performs the interpolations to adjust for the timing error. In the simulations performed for this thesis, the $L_{\mathrm{FF}} = 21$ is long enough to compensate for a timing error up to half a symbol time.

In conclusion, the CMA and DF-MMSE equalizers are able to compensate for the multipath interference encountered in aeronautical telemetry applications. These two equalizers present slight performance/complexity trade-offs than can be exploited to advantage. For both the waveforms, the DF-MMSE equalizer provided slightly better bit error rate performance than the CMA equalizer. This is somewhat expected since the CMA equalizer is completely blind while the DF-MMSE equalizer is not. The CMA equalizer requires a longer adaptive filter and must operate at a higher clock rate than the DF-MMSE equalizer, but the DF-MMSE equalizer requires training and at least course carrier phase synchronization.

## Bibliography


[1] C. Irving, "Range telemetry improvement and modernization," in *Proceedings of the International Telemetering Conference*, (Las Vegas, NV), pp. 294 – 303, October 1997.

[2] W. Gao and K. Feher, "FQPSK: A bandwidth and RF power efficient technology for telemetry applications," in *Proceedings of the International Telemetering Conference*, (Las Vegas, NV), pp. 480–488, October 1997.

[3] Range Commanders Council Telemetry Group, Range Commanders Council, White Sands Missile Range, New Mexico, *IRIG Standard 106-00: Telemetry Standards*, 2000. (Available on-line at http://jcs.mil/RCC/manuals/106-00).

[4] T. Hill, "An enhanced, constant envelope, interoperable shaped offset QPSK (SOQPSK) waveform for improved spectral efficiency," in *Proceedings of the International Telemetering Conference*, (San Diego, CA), pp. 127–136, October 2000.

[5] E. Law and K. Feher, "FQPSK versus PCM/FM for aeronautical telemetry applications; spectral occupancy and bit error probability comparisons," in *Proceedings of the International Telemetering Conference*, (Las Vegas, NV), pp. 489–496, October 1997.

[6] M. Goeghegan, "Description and performance results for the advanced range telemetry (ARTM) tier II waveform," in *Proceedings of the International Telemetering Conference*, (San Diego, CA), pp. 90–96, October 2000.

[7] T. Hill, "Performance of SOQPSK and multi-h CPM in the presence of adjacent channel interference," in *Proceedings of the International Telemetering Conference*, (Las Vegas, NV), pp. 255–263, October 2001.

[8] M. Rice, A. Davis, and C. Bettwieser, "A wideband channel model for aeronautical telemetry," *IEEE Transactions on Aerospace and Electronic Systems*, vol. 40, pp. 57–69, January 2004.

[9] J. Proakis, *Digital Communications*. McGraw-Hill, 2001.

[10] J. Treichler, "A new approach to multipath correction of constant modulus signals," *IEEE Transactions on Acoustics, Speech, and Signal Processing*, vol. ASSP-31, pp. 459–472, April 1983.

[11] J. Tu, "Optimum MMSE equalization for staggered modulation," in *Proceedings for the IEEE Asilomar Conference on Signals, Systems, and Computers*, vol. 2, (Asilomar, CA), pp. 1401–1406, November 1993.

[12] S. Kato and K. Feher, "XPSK: A new cross-correlated phase-shift-keying modulation technique," *IEEE Transactions on Communications*, vol. 31, pp. 701 –707, May 1983.

[13] M. Simon, *Bandwidth-Efficient Digital Modulation with Application to Deep Space Communications*. Wiley-Interscience, 2003.

[14] J. Anderson, T. Aulin, and C.-E. Sundberg, *Digital Phase Modulation*. New York: Plenum Press, 1986.

[15] M. Geoghegan, "Optimal linear detection of SOQPSK," in *Proceedings of the International Telemetering Conference*, (San Diego, CA), October 2002.

[16] S. Haykin, *Adaptive Filter Theory*. Prentice-Hall, 2001.

[17] J. C. H. J.R. Treicler, M. G. Larimore, "Practical implementations of blind demodulators," *IEEE*, pp. 1028–1032, 1998.